Environmental Science and Pollution Research (2023) 30:23938–23964
https://doi.org/10.1007/s11356-022-23690-6

RESEARCH ARTICLE

$MgO\text{-}La_2O_3$ mixed metal oxides heterostructure catalysts for photodegradation of dyes pollutant: synthesis, characterization and artificial intelligence modelling

Nawal Taoufik[1] · Fatima Zahra Janani[1] · Habiba Khiar[1] · Mhamed Sadiq[1] · Mohamed Abdennouri[1] · Mika Sillanpää[2,3,4,5] · Mounia Achak[6,7] · Noureddine Barka[1]

Received: 5 August 2022 / Accepted: 13 October 2022 / Published online: 4 November 2022

Abstract

In the present work, we prepared $MgO\text{-}La_2O_3$-mixed-metal oxides (MMO) as efficient photocatalysts for degradation of organic pollutants. First, a series of MgAl-%La-CO_3-layered double hydroxide (LDH) precursors with different contents of La (5, 10, and 20 wt%) were synthesized by the co-precipitation process and then calcined at 600 °C. The prepared materials were characterized by XRD, SEM–EDX, FTIR, TGA, ICP, and UV–vis diffuse reflectance spectroscopy. XRD indicated that MgO, La_2O_3, and $MgAl_2O_4$ phases were found to coexist in the calcined materials. Also, XRD confirms the orthorhombic-tetragonal phases of $MgO\text{-}La_2O_3$. The samples exhibited a small band gap of 3.0–3.22 eV based on DRS. The photocatalytic activity of the catalysts was assessed for the degradation of two dyes, namely, tartrazine (TZ) and patent blue (PB) as model organic pollutants in aqueous mediums under UV–visible light. Detailed photocatalytic tests that focused on the impacts of dopant amount of La, catalyst dose, initial pH of the solution, irradiation time, dye concentration, and reuse were carried out and discussed in this research. The experimental findings reveal that the highest photocatalytic activity was achieved with the $MgO\text{-}La_2O_3$-10% MMO with photocatalysts with a degradation efficiency of 97.4% and 93.87% for TZ and PB, respectively, within 150 min of irradiation. The addition of La to the sample was responsible for its highest photocatalytic activity. Response surface methodology (RSM) and gradient boosting regressor (GBR), as artificial intelligence techniques, were employed to assess individual and interactive influences of initial dye concentration, catalyst dose, initial pH, and irradiation time on the degradation performance. The GBR technique predicts the degradation efficiency results with $R^2 = 0.98$ for both TZ and PB. Moreover, ANOVA analysis employing CCD-RSM reveals a high agreement between the quadratic model predictions and the experimental results for TZ and PB ($R^2 = 0.9327$ and Adj-$R^2 = 0.8699$, $R^2 = 0.9574$ and Adj-$R^2 = 0.8704$, respectively). Optimization outcomes indicated that maximum degradation efficiency was attained under the following optimum conditions: catalyst dose 0.3 g/L, initial dye concentration 20 mg/L, pH 4, and reaction time 150 min. On the whole, this study confirms that the proposed artificial intelligence (AI) techniques constituted reliable and robust computer techniques for monitoring and modeling the photodegradation of organic pollutants from aqueous mediums by $MgO\text{-}La_2O_3$-MMO heterostructure catalysts.

Keywords $MgO\text{-}La_2O_3$ mixed oxides · Photocatalytic activity · Dye removal · Artificial intelligence (AI) · Gradient boosting regressor

Abbreviations

TZ	Tartrazine
ANN	Artificial neurol network
TGA	Thermogravimetric analysis
PB	Patent blue
RF	Random forest
ICP-MS	Inductively coupled plasma-mass spectrometry
AOP	Advanced oxidation processes
CCD	Central composite design
JCPDS	Joint Committee on Powder Diffraction Standards
UV	Ultraviolet
GBR	Gradient boosting regressor

Responsible Editor: George Z. Kyzas

✉ Nawal Taoufik
nawal.taoufik@gmail.com

Extended author information available on the last page of the article

MMO	Mixed metal oxides
ROS	Reactive oxygen species
BBD	Box-Behnken design
ANOVA	Analysis of variance
LDH	Layered double hydroxide
MATLAB	MATrix LABoratory
LOF	Lack of-fit
AI	Artificial intelligence
XRD	X-ray diffraction
MSE	Mean square error
RSM	Response surface methodology
SEM/EDX	Scanning electron microscopy/energy dispersive
X-ray	spectroscopy
VB	Valence band
LS-SVM	Least square-support vector machine
FT-IR	Fourier transform infrared
CB	Conduction band
MRGT50	Titanium dioxide/magnetite reduced graphene oxide
TiO_2/GO	Titanium dioxide/graphene oxide
MgP	Magnesium phosphate
Cu-mpg-C_3N_4	Copper nanoparticle-decorated mesoporous graphitic carbon nitride
TiHAp	Hydroxyapatite/titania nanocomposites
TiO_2/g-C_3N_4	Titanium dioxide/graphitic carbon nitride

Introduction

Water resources, especially surface water and groundwater, have become contaminated with organic substances as a result of increased population, urbanization, and a higher standard of living (Gijin et al. 2021; Abdi et al. 2022; Saharan et al. 2021; Sharma and Sharma 2013). Dyes are classified as a significant group of organic contaminants (Mariyam et al. 2021; Jain et al., 2014; Gupta et al. 2020; Sharma and Singh 2009). These pollutants are known to be released into different aquatic matrices through multiple pathways, including textile industry, paper, pharmaceutical industry, and bleaching industries (Su et al. 2020; Rizi et al. 2020; Quinto et al. 2020; Kumar et al. 2020). Each year, around $8 * 10^5$ tons of synthetic dyes are produced, with azo dyes accounting for half of them. Approximately 20% of this amount occurs in industrial effluents creating considerable concern and loading for effluent treatment systems (Bhagat et al. 2021; Mittal and Mittal 2015). The permanent release of these contaminants and their degradable precursors into the aquatic environment has harmful consequences for human health and deteriorates the whole ecosystem, exhibiting carcinogenic and mutagenic effects on living species (Balthazard-Accou et al. 2019; Han et al. 2016; Banu et al. 2019). These organic compounds are unable to be degraded by light or aerobic digestion; therefore, they require treatment before being released into the natural water matrices (Su et al. 2020; Rizi et al. 2020).

A number of methods have been developed for the removal of various kinds of dye from wastewater (Teotia et al. 2019; Gul et al. 2022; Januário et al. 2021). Some of these physico-chemical techniques chemical oxidation, flocculation/coagulation, ion exchange, membrane separation, and biological methods have been increasingly widely employed at present (Ismail and Sakai 2022; Bilinska and Gmurek 2021). However, these processes are principally constrained by the nonbiodegradable and toxic nature of the effluent, which reduces the efficiency of the process, and by the high quantities of solid waste produced, which needs the unnecessary contribution of other treatment processes which can hinder their widespread deployment (Barka et al. 2013; Taoufik et al. 2022). Adsorption and photodegradation have recently become two of the most promising techniques because they may effectively remove or adsorb these kinds of contaminant while also employing a low-cost and efficient process owing to their high oxidation capacity, strong stability, low toxicity, high flexibility, and cost-effectiveness (Ye et al. 2016). The good selection of the materials has considerable impact on the removal performance of these techniques. In this context, LDHs ($[M^{2+}_{1-x}M^{3}_{x}\ (OH)_2]^{x}\cdot(A^{n-}_{x/n})\cdot mH_2O$) have gained a lot of interest as potential materials for wastewater treatment as an adsorbent or catalyst owing to their attractive features such as their unique structure, tunable bandgaps, ease of scaling, low cost, high surface area, tunable optical bandgap (2.7 eV), and excellent thermal and chemical stability (Mittal 2021). Some reports of LDH application as adsorbents of wastewater dye pollutants and their adsorptive performance are listed in Table 1. In another aspect, LDHs have been extensively researched as catalysts and catalyst precursors to degrade organic contaminants such as dyes over the past decades. Since the calcination of hydrotalcite-like materials produced mixed metal oxides, they are reported to also have a homogeneous dispersion of M^{2+} and M^{3+} at an atomic level, a high specific area, good photocatalytic activity, and other fascinating physical and chemical properties (Elhalil et al. 2019; Ghemit et al. 2017; Cocheci et al. 2020). Consequently, mixed metal oxides from the calcination of hydrotalcites have been evaluated for different catalytic applications. Meanwhile, other examples regarding the employments of LDH-based material catalysts in the photodegradation of dyes are presented in Table 2.

Tartrazine (TZ) and patent blue (PB) anionic azo dyes are the most widely used compounds as an additive in textile, cosmetics, and food industries (Soufi et al. 2022; Machrouhi et al. 2022). Although PB is easily degradable, it can provoke harmful impacts such as asthma, headaches, and allergic reactions (Sadiq et al. 2021; Barka et al. 2011; Mittal

Table 1 Comparison for the adsorption efficacy (q_{max}) of dyes by different LDH-based materials

LDH	Preparation	Pollutants	Adsorption capacity (mg/g)	Ref
Zn-Al-LDH	Coprecipitation	Methyl orange	540.1	Li et al. (2020)
Magnetite-nano-particle-Ni–Fe LDH	Coprecipitation	Congo red	94.3	Taher et al. (2021)
Zn_2Al-Cl-LDH	Coprecipitation	Tartrazine	282.48	Ouassif et al. (2019)
Ni–Fe-SDS-LDH	Coprecipitation	Methyl orange	106.18	Elmoubarki et al. (2021)
Mg–Al-LDH	Coprecipitation	Acid Orange 7	485.6	Pan et al. (2020)
Zn/Al/Fe-LDH	Coprecipitation	Indigo Carmen	160	Bessaha et al. (2017)
Zn-Al-CO_3-LDH	Mechanochemical	Methyl orange	193.82	Ai et al. 2018
Mg-Fe-CO_3-LDH	Coprecipitation	Methyl orange	95.10	Elmoubarki et al. (2017)
Ni-Mg–Al-LDH	Coprecipitation	Eriochrome black T	156.25	Kazeem et al. (2020)
Zn-Al-CO_3-LDH	Microwave-assisted hydrothermal	Congo Red	571.43	Srilakshmi and Thirunavukkarasu (2019)
S-Mg/Al LDH	Coprecipitation	Tartrazine	131.9	Grover et al. (2022)

Table 2 Photocatalytic performances of some LDH-based materials for the degradation of dyes in aqueous medium

LDH	Preparation	Catalyst dose (g/L)	Pollutants	Irradiation time (min)	Degradation (%)	Ref
Zn-Ti-LDH	Co-precipitation	1.0	Methylene blue	100	~100	Shao et al. (2011)
Zn-AL-LDH	Hydrothermal	1.0	Rhodamine B	60	94	Zhang et al. (2019)
ZnO-LDH@C_3N_4	Co-precipitation/Solvothermal	1.0	Methylene blue	240	~100	Zhang et al. (2016)
Co-Cr-CO_3-LDH	Co-precipitation	1.0	Methyl orange	180	90	Baliarsingh et al. (2014)
Cu-Co-Cr-LDH	Co-precipitation	0.2	Malachite green	240	90	Parida et al. (2013)
C_3N_4/ZnAl-LDH	In situ crystallization	1.0	Methylene blue	240	98	Yuan and Li (2017)
Salen-M-ZnCr-LDH	Co-precipitation	1.0	Rhodamine B	420	90	Meng et al. (2017)
Ni–Fe-LDH	Hydrothermal	1.0	Congo Red	300	91.1	Suppaso et al. (2021)
Zn-Al-Ce-MMO	Co-precipitation	0.5	Rhodamine B	240	97.8	Zhu et al. (2016)
CdS/CoAl-LDH	Hydrothermal/anion-exchange	1.0	Rhodamine B	60	100	Cai et al. (2017)
N-TiO_2/ZnAl-MMO	Adsorption-sol–gel	1.0	Methyl orange	30	96,2	An et al. (2015)

2020; Costa et al. 2020). Tartrazine, also known as E102, is a yellow azo dye that is approved for use as a food additive in the European Union (EU) at a standard daily dose of 0–7.5 mg/kg bw/day. Contrary to PB, TZ is considered a recalcitrant compound and also has adverse effects on the health of humans causing depression, anxiety, migraine, asthma attacks, sleep disorders, and anaphylactic shock (Lacson et al. 2022). Also, it is claimed that the consumption of this kind of dye also referred to as "yellow 5" can have a negative effect on the activity and attention of children (Mittal 2020). Therefore, it is crucially important to treat the wastewater containing these dyes before discharged into the aquatic environment (Zubair et al. 2022; Ali et al. 2022).

Another part of our work is devoted to modeling. In fact, one of the main principles in the design of any wastewater technology is the determination of the optimal conditions of the process. Photocatalysis is one of the water purification technologies that involve a series of experiments to learn more about the effects of input variables, which can be both time-consuming and expensive. It would therefore be interesting to develop general predictive techniques to analyze dye removal and to discover the relative importance of each variable and their interactions on removal capacity. One of the possible approaches to model processes of great complexity is the exploitation of artificial intelligence (AI) techniques. These empirical methods are characterized by total independence of information about the process concerned which allows to map the nonlinear behaviors between a group of input and output parameters. Various AI techniques have been used for the estimation and modeling of removal of dyes, such as response surface methodology (RSM) (Fetimi et al. 2021), random forest (RF) (Soares et al. 2020), least square-support vector machine (LS-SVM) (Ghaedi et al. 2014), and

artificial neurol network (ANN) (Mossavi et al. 2022). For instance, Soares et al. (2020) reported the feasibility of RF and ANN to model the adsorption process of methylene blue, which is considered a well-known AI technique in this field. Based on the obtained results, both RF and ANN models exhibited similar performances.

RSM via central composite design (CCD) and gradient boosting regressor (GBR) model are examples of AI tools that have been exploited in the present research. RSM is a commonly applied statistical tool for modeling and optimization of overall contributions from all variables. At the same time, it reduces the number of experiments while enhancing the performance of the multicomponent processes with the minimum of experimentation errors, and it provides scientists with a simple, convenient, and innovative procedure that can be rapidly implemented. Among the RSM models employed by researchers for modeling the multicomponent systems which include the Box-Behnken design (BBD), central composite design (CCD), the historical data design, and the user-defined design (Zhang et al. 2018a, b; Kooh et al. 2022; Friedman et al. 2000).

On the other hand, GBR is considered a very attractive and robust AI tool explaining complex nonlinear problems between input and output sets, owing to its flexibility in determining relationships between factors in smaller data sets and at the same time its ability to manage a large number of input variables (Wei et al. 2019; Mazaheri et al. 2017). Furthermore, its capability has been verified as being capable of solving a variety of engineering datasets.

The evolutionary scalability of the GBR technique is determined by optimizing multiple critical models and algorithms, such as a robust new tree-based learning algorithm for processing sparse data and a reasonable weighted algorithm for data management.

In the first phase of this study, MgAl-CO_3 and a series of MgAl-%La-CO_3 LDHs with different La contents at Mg/(Al + La) molar ration of 3 were prepared through coprecipitation process and calcined at 600 °C in a tube furnace. The as-synthesized materials MgO-Al_2O_3-MMO and (MgO-La_2O_3 (5, 10, 20%)-MMO) were used as photocatalysts for the degradation of TZ and PB as a model of textile contaminants under UV–visible irradiation. Many operating variables, including dye concentration, pH of the solution, catalyst doses, and reaction time, have been used to assess the as-synthesized material's ability to degrade the dyes. The RSM (using CCD plane) and GBR for prediction and optimization of the performance of the photodegradation process using the prepared materials were constructed in the second stage of the work based on MATLAB and Design-Expert software.

Materials and methods

Reagents

All reagents were used in the commercial form, without further purification. The chemicals employed for the synthesis of hydrotalcites were as follows: magnesium nitrate ($Mg(NO_3)_2{\cdot}6H_2O$), aluminum nitrate ($Al(NO_3)_3{\cdot}9H_2O$), lanthanum nitrate ($La(NO_3)_3{\cdot}6H_2O$), and sodium carbonate (Na_2CO_3) were products of Sigma-Aldrich, and NaOH used for pH adjustment was purchased from Labo Chemie (Spain). The target pollutant compounds, that is, TZ ($C_{16}H_9N_4Na_3O_9S_2$, 214.65 g/mol, $pK_a = 9.4$) and PB ($C_7H_6O_3$, 138.12 g/mol, $pK_a = 2.78$), were purchased from Sigma-Aldrich.

Synthesis of LDH precursors and the MgO-La_2O_3-MMO photocatalyst

MgAl-%La-CO_3 LDHs were prepared through the coprecipitation procedure using a 3:1 molar ratio with La contents of 0, 5, 10, and 20% at a constant pH solution. Typically, in 150 mL of deionized water, a mixed solution of Mg $(NO_3)_2{\cdot}6H_2O$, $Al(NO_3)_3{\cdot}9H_2O$, and $La(NO_3)_3{\cdot}6H_2O$ with a total metal ion concentration of 2 mol/L was dissolved. Subsequently, the alkaline solution Na_2CO_3 (50 mL, 1 mol/L) was added to a stirred mixed nitrate solution in a beaker containing 50 mL of double-distilled water. To maintain a constant pH value of about 8.7 ± 0.2, a suitable amount of NaOH solution (2 M) was also added dropwise under vigorous stirring. The formed gel was kept under continuous stirring for 4 h and then placed in an autoclave submit to a hydrothermal treatment for 16 h at 75 °C to produce a structure for LDHs that is well-crystallized.

After that, the obtained precipitates were filtered and washed repeatedly using bidistilled water in order to remove any ions that may have remained in the finished products, and then aged at 100 °C for 16 h to obtain MgAl-La CO_3 LDHs with various contents of La (0, 5, 10, and 20%); these precursors were denoted as MgAl-La-CO_3-LDH, where *z* represents the content weight percentage of La(III). Finally, LDH samples were calcined at 600 °C for 6 h, to obtain MgAl-La mixed-metal oxides, which were named MgO-La_2O_3 MMO. In this research, the mixed-metal oxide with different contents of La (5, 10, and 20 wt%) was denoted specifically as MgO-La_2O_3-5% MMO, MgO-La_2O_3-10% MMO, and MgO-La_2O_3-20% MMO.

Characterization techniques

The structural, textural, and morphological characteristics of the as-synthesized products were evaluated by X-ray diffraction, scanning electron microscopy (SEM), Fourier transform infrared (FTIR), ICP, and thermogravimetric analysis (TGA). The X-ray diffraction (XRD) patterns of the LDH precursors and their calcined products were realized at room temperature on a D2 PHASER diffractometer coupled with Cu Kα radiation ($\lambda = 1.5418$ Å) at 30 kV and 10 mA. The patterns were recorded in a 2-h range from 5 to 70, in a step size of 0.01° (0.5 s/step), and Scherrer's formula was used to determine crystallite size (Eq. 1):

$$D = \frac{K\lambda}{\beta\cos(\theta)} \quad (1)$$

where D represents the crystallite size (nm), k is a constant (0.9), λ corresponds to the wavelength used (0.15406 nm), β is the peak width at half maximum in radian along the (101) plane, and θ represents the diffraction angle. The shape and size of the as-prepared samples were observed using SEM coupled with an energy-dispersive X-ray spectroscope (SEM/EDX) on a FEI FEG 450 (Tescan) instrument. FT-IR spectra were recorded with a PerkinElmer FT-IR spectrophotometer, in a range of 4000–400 cm^{-1}, and the products were pressed into KBr disks. Thermogravimetric analysis (TGA) was carried out by using a TGA-Q500 equipment. The samples were submitted to heating from room temperature to 900 °C with a heating rate of 10 °C/min using nitrogen as a sweep gas at a flow rate of 90 mL/min. Furthermore, the elemental composition of the synthesized particles was measured by using an inductively coupled plasma utilizing an ICP-MS (Varian 2011) spectrometer.

Adsorption/photocatalytic degradation

To perform the photodegradation experiments, 100 mL of TZ solution (20 mg/L) containing 50 mg of each catalyst was added to a 100-mL glass beaker, then it was placed under ultraviolet and visible light (UV–Visible) irradiation by a 400-W halogen lamp for 180 min, located 10 cm above the cell. The lamp was positioned inside a quartz vessel with two compartments: one containing the lamp and the other transmitting the water in a recirculation channel for temperature control and cooling of the system. It is worth mentioning that for every experiment, the adsorption tests, without irradiation, were performed for 1 h in order to achieve the adsorption–desorption equilibrium between the surface of the catalyst and dye. Therefore, the influence of surface adsorption in the degradation of TZ and PB is eliminated. Furthermore, the photolytic degradation tests (direct photolysis), in the absence of photocatalysts, were also carried out under similar operating conditions.

The effect of dye concentration using 0.3 g/L of MgO-La_2O_3-10% MMO was assessed by varying its concentration from 10 to 20 mg/L for TZ and PB. The photocatalyst dose was changed from 0.1 to 0.7 g/L, keeping the pH value at 4.05 and the TZ and PB dye concentrations at 20 and 10 mg/L, respectively. The effect of the pH was evaluated at pH values of 4, 6, and 9 (adjusting using NaOH (0.1 N) and HCl (0.1 N)).

At regular time intervals, 4-mL aliquots were taken and subsequently filtered to separate the catalysts. The residual concentration of TZ was defined by using a TOMOS V-1100 UV–Vis spectrophotometer at its maximum adsorption wavelength of $\lambda_{max} = 425$ nm. The same procedure and concentrations were used for (PB) ($\lambda_{max} = 637$ nm). All adsorption/photodegradation experiments were performed at least twice, and the results are reported as an average.

Computational details

Design of experiments

To evaluate the influence of the efficient factors and also identify the optimal conditions for the photocatalytic degradation efficiency of both dyes TZ and PB using %La-MgO-Al_2O_3, the RSM design-CCD design was designed applying Design Expert Software (version 11). The RSM is a statistical and mathematical tool used for analyzing the impact of independent factors on the response and developing the regression model equations, which are useful for reaching the best system efficiency. Additionally, RSM investigated the influence of interactions and relations between effective operating variables on the photocatalytic degradation efficiency of TZ and PB to achieve the best conditions. In this research, the effect of four variables and five levels, initial dye concentration (mg/L) (X_1), pH (X_2), photocatalyst dosage (g/L) (X_3), and reaction time (min) (X_4), was observed. The observed response is the degradation efficiency of the dyes after 180 min (R, %).

While regarding all the possible combinations of the input variables, RSM analysis suggested 30 experiments in total for each dye, among which 6 replications to a central point aimed at the correct optimization of the data, and a quadratic model was used to explore the interaction between the independent and dependent factors. The experimental intervals and different levels of experimental designs for both dye removal envisaged in this research are illustrated in Table 3. To perform statistical calculations, the experimental variables X_i were coded as x_i based on the following transformation equation:

Table 3 Experimental range and levels of independent process factors

Variables	Ranges and levels					ΔX
	−2	−1	0	1	2	
Initial dye concentration (mg/L) (X_1)	5	10	15	20	25	5
pH (X_2)	3	4	5	6	7	1
Photocatalyst dosage (g/L) (X_3)	0.2	0.3	0.4	0.5	0.6	0.1
Reaction time (min) (X_4)	90	110	130	150	170	20

$$X_i = \frac{x_i - x_0}{\Delta x} \quad (2)$$

where X_i represents the uncoded value of the ith independent parameters and x_i is the dimensionless coded value of the ith independent parameters, x_0 is the value of x_i at the center point, and Δx presents the step change value of the actual parameter.

Gradient boosting regression modeling

The GBR is an ensemble learning algorithm which was developed further by Friedman (Friedman et al. 2000). The GBR is an optimization algorithm that is employed to solve classification and regression problems (Wei et al. 2019). It is able to generate a strong prediction model by combining weak prediction models, that is, the decision tree. The key principle is that each calculation is performed by a base model, and the next calculation is taken to reduce the residual of the last model and make a new base model in the direction of the gradient with reduced residuals.

The tuning of the GBR model involves the setting of several hyperparameters including max_depth, min_samples_leaf, and allowing to set it as n_estimators.

Various studies investigated the performance of GBR in the prediction of various pollutants. Mazaheri et al. (2017) evaluated the performance of the AI algorithm GBR for modeling the adsorption of methylene blue and Cd(II) and then compared it with the neural network (ANN) method. They found that both approaches have comparable performance, which means that both models have the potential to predict the response of the studied process. In the same vein, Hanandeh et al. (2021) employed six AI models that were developed and evaluated to predict heavy metal adsorption in single, binary, and ternary environments. All models provided outstanding results, with the correlation coefficient between the predicted and expected values > 0.99 in all cases. The findings of this study also demonstrated that the GBR model can be employed for the prediction of experimental data and can be useful in reducing the cost of the experiment. In another study, Bhagat et al. (2020) explored the prediction of the adsorption performance of Mn by GBR. They have proven the robustness and predictive ability of this methodology.

Results and discussion

Characterization of catalysts

X-ray diffraction

The XRD analysis was realized to recognize the phase structure of the prepared materials. Figure 1 illustrates the X-ray

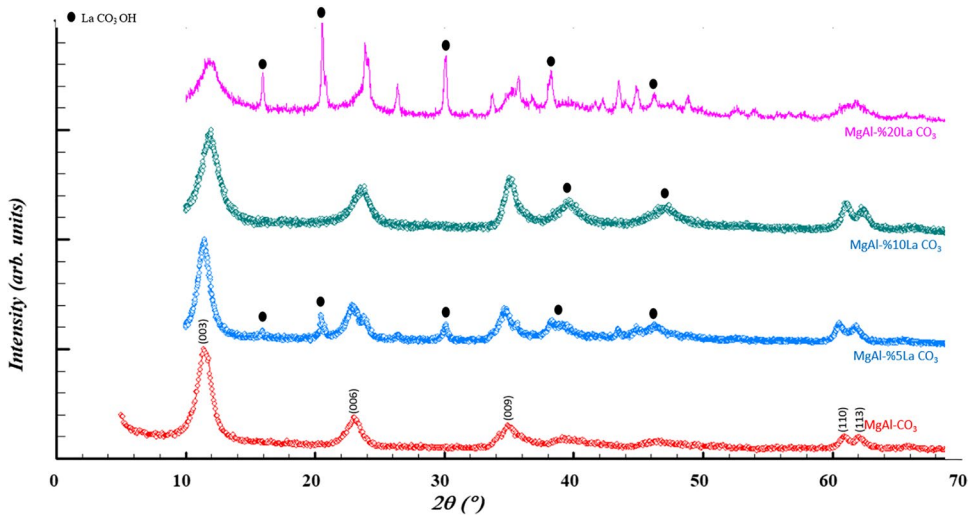

Fig. 1 X-ray diffractograms for Mg–Al-LDH, Mg–Al-La-5%-LDH, Mg–Al-La-10%-LDH, and Mg–Al-La-20%-LDH

diffraction patterns of LDH precursors. It can be seen that all LDH precursors exhibit identical, typical sharp and strong reflections, implying good crystallinity. The XRD patterns of MgAl-%La-CO_3LDHs revealed that the recognized peaks were matched to MgAl-CO_3 LDH patterns and they have the appearance of a layered structure, which reveals that the presence of La in the samples does not cause the layered structure to be destroyed, whereas the intensity of the peaks decreases proportionally with the lanthanum(III) content.

The diffraction peaks at 11.42, 23.04, 34.29, 60.97, and 62.04° 2θ could be attributed to the (003), (006), (009), (110), and (113) reflections of LDH, respectively, characteristic of a layered structure, without any independent Mg or Al phases (JCPDS 70–2151). These findings reveal that MgAl-%La-CO_3-LDHs can be successfully synthesized with varied contents of La (5, 10, and 20 wt%). Almost similar typical structures were observed in the XRD profiles of the precursors MgAl- 5%La-CO_3, MgAl- 10%La-CO_3, and MgAl- 20%La-CO_3 and were in agreement with those of natural hydrotalcite (card JCPDS 40–0216); in this case, La^{3+} ions substitute for Al^{3+} ions. The characteristic XRD peaks of $LaCO_3$ OH started to appear as indicated by the peaks at 2θ = 15.87, 22.3, 30.23, 38.4, and 46.32° (JCPDS 36–1481).

The fineness and crystallinity as a measure of reflection intensity decreased with increasing lanthanum content. Although MgAl-20%La CO_3 still has the main characteristic of LDH, the by-products have been produced. On the other hand, there were no diffraction bands for these lanthanum species in the XRD pattern of MgAl-5%La CO_3. This suggested that lanthanum species may be widely dispersed on the surface of catalysts in modest amounts that XRD could not detect. The possible reason may be related to the different charge densities for La^{3+} and Al^{3+} ions. The La^{3+} has lower charge density compared to Al^{3+} owing to its larger ionic radius; as a result, the probable insertion of La^{3+} into the hydroxide sheets would cause the octahedral structure to be distorted, resulting in the formation of a new phase. The high electric charge of lanthanum favored the formation of carbonate and oxyhydroxide lanthanum species at the very early step of the co-precipitation; thus, its high ionic radius inhibited the intercalation of larger lanthanum species in the hydrotalcite structure (Guo et al. 2012).

The XRD patterns of the LDH precursors after the calcination at 600 °C (see Fig. 2) indicated that the reflections associated with LDHs had completely disappeared and that some new ones had been observed after the calcination of MgAl-La-CO_3 LDHs, signifying the collapse of the lamellar structure. The characteristic XRD peaks of MgO oxide began to appear as illustrated by the reflections at 43.72 and 63.45° 2θ, whereas there is a detection of signals corresponding to the $MgAl_2O_4$ phase at 36.93, 44.8, 59.4, and 65.2° 2θ. This is also supported by the JCPDS data (Card No. 21–1152).

By increasing the La content, the characteristic peaks are observed at 2θ of 29.73, 35.51, 51.68, and 54.65 confirming the formation of La_2O_3 without an obvious new phase containing La^{3+} or Al^{3+} (JCPDS No. 05–0602). The phase La_2O_3 is produced from the thermal decomposition of the relative species of lanthanum carbonate and oxyhydroxide by calcination at 600 °C K (Sahnoun et al. 2018), hence the presence of peaks at 2θ angles of 13.23°, 22.97°, and 43.18° confirming the formation of the monoclinic lanthanum dioxycarbonate $La_2O_2CO_3$ phase (JCPDS 48–1113) (Kiwaan et al. 2020; Elhalil et al. 2018). However, there is no detection of signals related to the Al_2O_3 phase, which signifies that Al_2O_3 was amorphous.

The crystallite size for Mg–Al-LDH and Mg–Al-La-10%-LDH was calculated to be 260 Å and 382.7 Å, respectively, and this confirms the loading of lanthanum. Moreover, after calcination treatment, the crystallite size increased from 260 to 97.20 Å for Mg-Al-LDH and

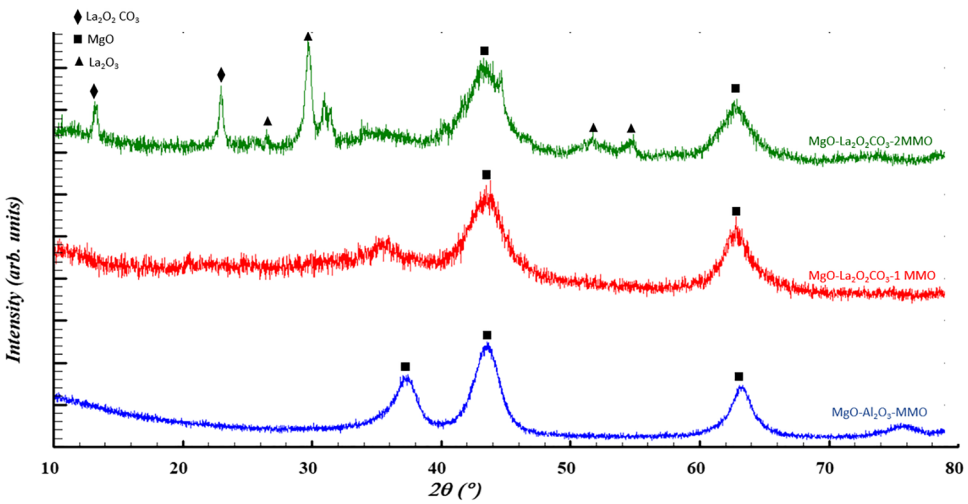

Fig. 2 XRD patterns calcined LDH materials at different 600 °C: MgO-Al_2O_3-MMO, MgO-La_2O_3-5% MMO, and MgO-La_2O_3-10% MMO

Mg-Al-10%La-LDH and from 382 to 482.34 Å for MgO-Al_2O_3-MMO and MgO-La_2O_3-10% MMO, respectively.

Fourier transform infrared spectra

The functional groups of the prepared materials were determined by the FTIR spectra. Infrared spectroscopy of LDH precursors before and after calcination at 600 °C are presented in Figs. 3 and 4. The absorption peak between 3314 and ~ 3682 cm^{-1} in the spectra of the LDH materials was attributed to the stretching vibration of the OH group with hydrogen bonding from interlayer water molecules. Another typical band for the LDH materials is observed at 1626 cm^{-1}, which was assigned to the O–H bending vibration of water molecules. An absorption peak at 1372 cm^{-1} was ascribed to the stretching vibration of the carbonate anions CO_3^{2-}. In the low-frequency region, the peaks observed in the range of 500–870 cm^{-1} could be assigned as lattice vibration modes of metal–oxygen-metal vibration (M–O, M-OH). The difference in the infrared spectra compared to the noncalcined materials could be attributed to the difference in the structure of the compounds constituted with different amounts of La. It can be observed that after calcination ($T = 600$ °C), the typical CO_3^{2-} bands (1364 cm^{-1}) are still present. This band is assigned to the formation of the $La_2O_2CO_3$ phase.

Thermogravimetric analysis

Thermal analysis, such as thermogravimetric analysis (TGA), is a recognized technique for observing the decomposition reactions or physical and chemical reactions of the prepared materials. The thermal stabilities of the MgAl-CO_3-LDH and MgAl-La-10%-LDH were performed as a function of the temperature by TGA, and the findings

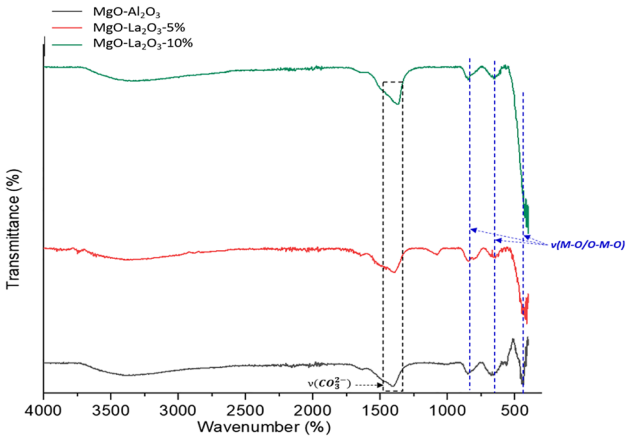

Fig. 4 FTIR spectra of the calcined LDH materials at 600 °C

are illustrated in Fig. 5. Accordingly, the TGA curve of MgAl-CO_3LDH exhibits three well-distinguished degradation parts. The first part is associated with the removal of water at the surface of the LDH interlayer (45–195 °C), and a weight loss of 16.65% is displayed on the TG curve for this part. The second one (in the temperature range of 195–275 °C) is associated with dehydration of the brucite-like layers, where the TGA curve indicates a smaller weight loss of 2.31%. The last weight loss of 9.2% also occurred at a temperature range of 275–505 °C, which is attributable to the decomposition of interlayer carbonates ions and dehydroxylation of the MgAl-CO_3LDH layers. The total mass loss of the synthesized LDH sample was determined to be 28.16%. MgAl-10%La-CO_3LDH and MgAl-CO_3LDH display a similar behavior. The temperature range for the first mass loss for MgAl-10%-La-CO_3LDH which extended up to 185 °C is assigned to the dehydration of residual water molecules from the

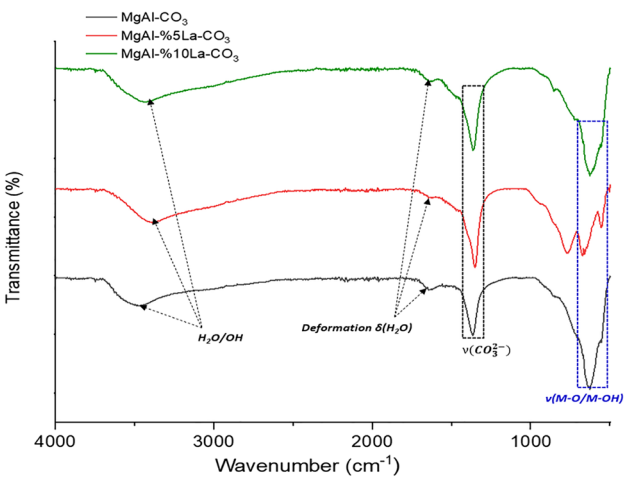

Fig. 3 FTIR spectra of the fresh LDH precursor

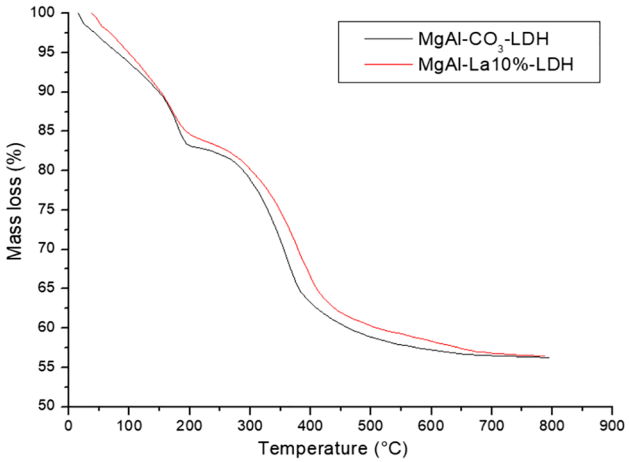

Fig. 5 Thermogravimetric analysis of the MgAl-CO_3-LDH and MgAl-%10La-CO_3 LDHs between 25 and 800 °C

synthesized material surface. In the second degradation step at the central temperature range 185–245 °C, a gentle mass loss was observed of about 2.57%, due to dehydroxylation of the metal hydroxide layers. A third step, which was observed between 405 and 505 °C, is assigned to the de-carbonation that occurred.

SEM analysis

The surface morphologies and microstructure of the as-prepared samples MgAl-%La-CO_3 LDHs with different contents of La and the corresponding mixed oxide samples were examined through a SEM and the corresponding EDX spectrum, as displayed in Fig. 8. It is clearly seen that the MgAl-CO_3 LDH showed a particle aggregation and the corresponding EDX spectrum showed the presence of Mg and Al also indicating that LDH was successfully synthesized. The SEM image of MgAl-%La-CO_3 LDHs (see Fig. 6 b–d and h) has a heterogeneous surface with clearly observable porosity with a particle size range of 75–125 nm which was obtained from ImageJ software usage. The La particles were randomly and highly dispersed on the surface of the MgAl-CO_3 LDH. The MgAl-CO_3LDH sample exhibits the same morphology as the MgAl-%La CO_3 LDH but with larger clusters. The EDX pattern further confirmed the presence of Mg, Al, and La in MgAl-%La-CO_3 LDHs. When MgAl-%La-CO_3 LDHs are calcined at 600 °C, their agglomeration in the form of a sponge is more evident and crystallization of the oxide occurred forming large particles which are responsible for the increase in the catalyst surface heterogeneity (the heterogeneity of the surface). In this manner, the particle size range of calcined MgAl-%La-CO_3 was obtained at 100–150 nm.

For the MgO-La_2O_3-(5, 10, 20%) MMO, the spectrum exhibits peaks associated with La along with the other component elements Mg, Al, and O.

Chemical composition analysis

The analysis of the chemical composition of the LDH precursors was performed by ICP-MS. The synthesized materials were dissolved in an acidic bath employing 63% of concentrated nitric acid. The obtained results are displayed in Table 4. Based on the analysis, as expected, the MgAl-%La LDH is composed essentially of magnesium, aluminum, and lanthanum. The molar ratio of (La/Al) was found to be 0.051, 0.123, and 0.26 for MgAl-5%La-CO_3 LDH, MgAl-10%La-CO_3 LDH, and MgAl-20%La-CO_3 LDH, respectively, which are slightly higher than the theoretical values (see Table 2).

UV–vis

The optical absorption spectra of the as-synthesized materials MgO-Al_2O_4-MMO and MgO-La_2O_3-10% MMO were evaluated by UV–vis diffuse reflectance spectroscopy (UV-DRS), and the results are presented in Fig. 7. The sample MgO-Al_2O_4-MMO shows two absorption bands that are consistent with the data presented for $MgAl_2O_4$ prepared by another method (Mossavi et al. 2022). The MgO-La_2O_3-10% MMO sample exhibits a strong absorption band at 300 nm with its absorption edge extending to 550 nm, which gives a band gap of 3.05 eV. The absorption of the MgO-La_2O_3-10% MMO is apparently higher than that of the MgO-Al_2O_3-MMO in the range of 200 to 800 nm, which means that the absorbance band increases with the incorporation of La in the lattice. This remarkable photo-adsorption enhancement of the MgO-La_2O_3-10% MMO stems from the incorporation of La particles, confirming the existence of La species in the product. It was interesting to observe that the MgO-La_2O_3-10% MMO might have higher photocatalytic activity under visible light irradiation. The rate of electron hole pair production on the surface of the catalyst rises with rising absorption intensity, resulting in enhanced photocatalytic performance. The band gap energies of the samples MgO-Al_2O_3-MMO and and MgO-La_2O_3-10% MMO were determined based on the start of the UV–vis spectra of the absorption values (Eq. (3)).

$$(ahv)^2 = k(hv - E_g) \tag{3}$$

where the terms a, h, ν, K, and E_g represent the absorption coefficient, Planck's constant (J·s), light frequency (s^{-1}), absorption constant, and band gap of semiconductors (eV), respectively.

The average band gap energies for MgO-Al_2O_3-MMO and MgO-La_2O_3-10% MMO were thus calculated to be 3.22 and 3.05 eV, respectively. It can be concluded that the MgO-La_2O_3-10% MMO has a lower band gap energy and is expected to present better photocatalytic activity under visible light compared with MgO-Al_2O_3-MMO. The lower band gap could be assigned to the composite oxides formed by calcination of MgO, La_2O_3, and $MgAl_2O_4$ and the coupling interaction among their phases, and the form of the heterojunction structure, resulting in an improvement in light utilization and photocatalytic performance.

Photocatalytic study

In an attempt to evaluate the photocatalytic activities of the catalysts (MgO-La_2O_3- (5, 10, 20%)-MMO), photocatalytic degradation of 20 ppm TZ and PB solutions by the catalysts was performed under ultraviolet–visible irradiation.

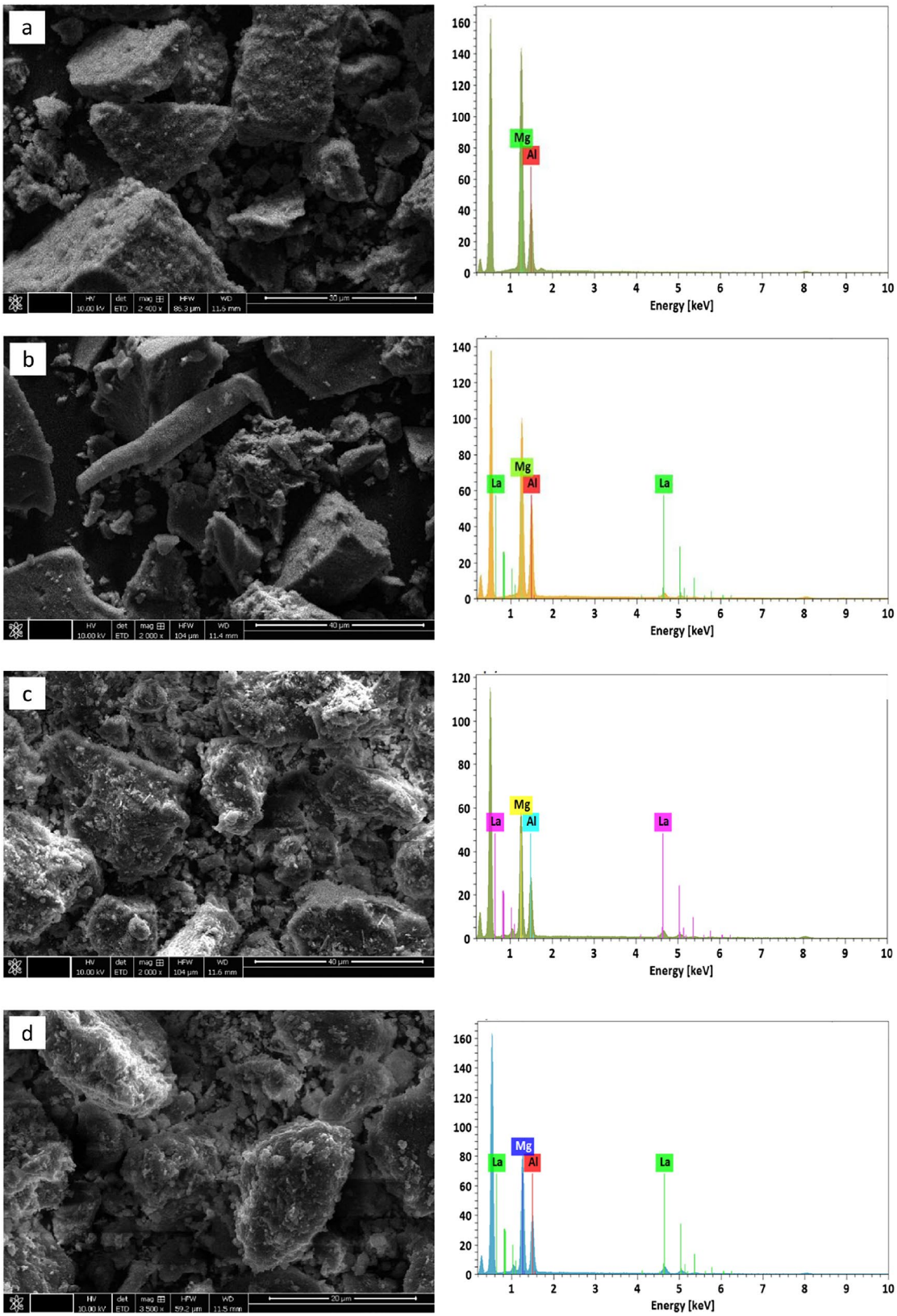

Fig. 6 SEM–EDX images of **a**–**d** MgAl-CO_3 LDH, MgAl-5%La-CO_3 LDH, MgAl-10%La-CO_3 LDH, and MgAl-20%La-CO_3 LDH, and **e**–**g** MgO-La_2O_3 5% MMO, MgO-La_2O_3 10% MMO, and MgO-La_2O_3 20% MMO. Diameter distributions of **h** 10%La-CO_3 LDH and **i** MgO-La_2O_3 10% MMO

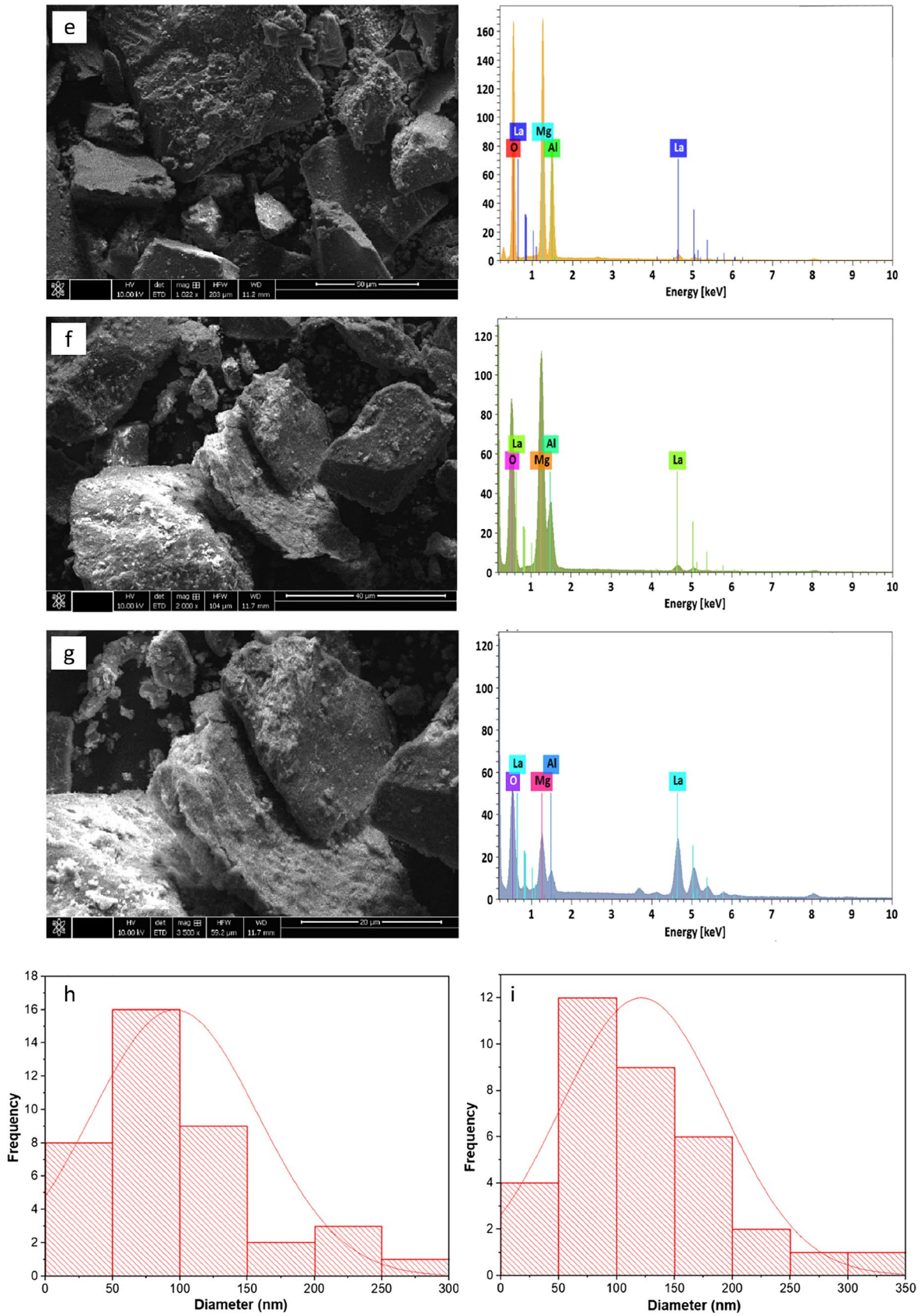

Fig. 6 (continued)

Table 4 Elemental compositions of LDH precursors determined by ICP-MS analysis

	Cu (%)	Mg (%)	Fe (%)	Zn (%)	Al (%)	La (%)	Ni (%)
MgAl-CO_3	0.0037	42.1160	0.0079	0.0001	12.3503	0.0006	0.0061
MgAl-5%La-CO_3	0.0017	40.1160	0.0030	0.0004	6.6928	0.3420	0.0004
MgAl-10%La-CO_3	0.0053	42.7840	0.0220	0.0001	5.2050	0.6422	0.0013
MgAl-20%La-CO_3	0.0030	43.2150	0.0062	0.0002	5.4814	1.4307	0.0024

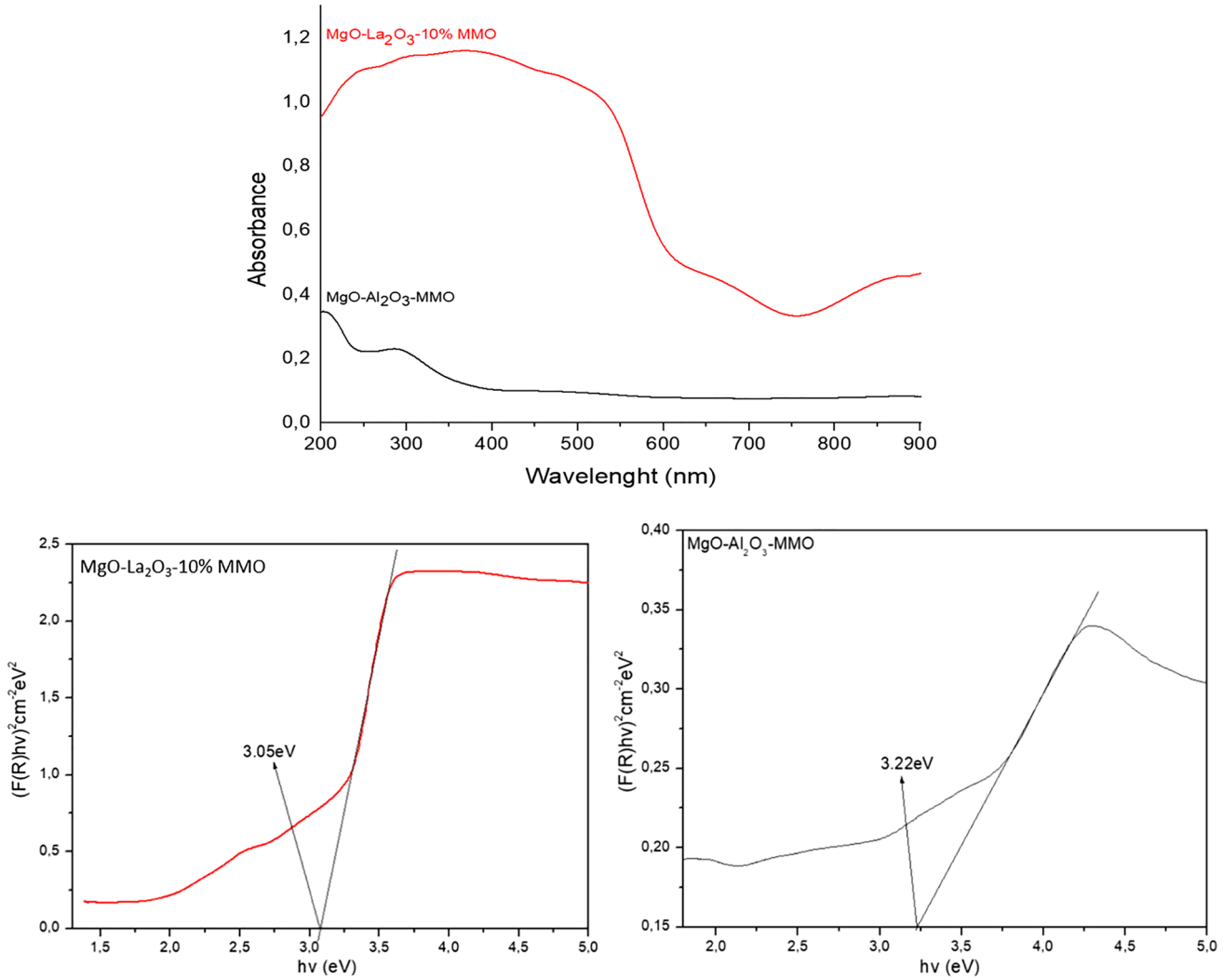

Fig. 7 UV–vis diffuses reflectance spectra and bandgaps of MgO-Al_2O_3-MMO and MgO-La_2O_3-10% MMO

Degradation of the dyes was determined by measuring the absorbance of the dye solutions in 30-min intervals for 3 h.

Effect of the La doping on the photocatalytic reaction

The photocatalytic performance of the MgO-La_2O_3 (5, 10, 20%) MMO with different La doping contents was examined by the photodegradation of two dyes TZ and PB under ultraviolet–visible irradiation in the same photocatalytic experiments. The present section involves the photocatalytic activity of MgO-La_2O_3 (5, 10, 20%) MMO compared to MgO-Al_2O_3-MMO as references which has been investigated. The photolytic degradation (direct photolysis) without photocatalysts was investigated under the same operating conditions as photocatalytic degradation. Figures 10 and 11 present the results of photocatalytic activities of different catalysts. It can be clearly seen that the degradation of TZ and PB is very insignificant in the absence of photocatalysts under ultraviolet–visible irradiation.

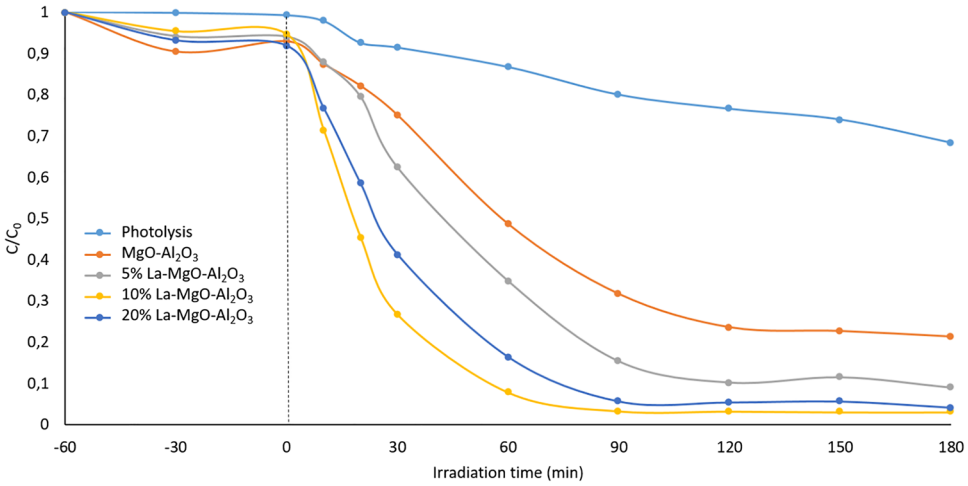

Fig. 8 Adsorption/photocatalytic degradation of TZ in the presence of the synthesized samples (TZ concentration: 20 mg/L; photocatalyst dosage: 0.3 g/L; irradiation time: 150 min, and pH ~ 4.08)

In the adsorption phase, MgO-La_2O_3-5% MMO and MgO-La_2O_3-10% MMO have hardly any adsorption of TZ after being stirred for 60 min. The adsorption efficiencies of TZ on MgO-Al_2O_3 MMO, MgO-La_2O_3-5% MMO, MgO-La_2O_3-10% MMO, and MgO-La_2O_3-20% MMO are 9.57%, 5.85%, 4.65%, and 6.85%, respectively. Clearly, MgO-Al_2O_3 MMO exhibits a slightly higher adsorptive ability than other photocatalysts. While the adsorption process decreases in the presence of MgO-La_2O_3-5% MMO and MgO-La_2O_3-10% MMO catalysts, respectively. On the other hand, Figs. 8 and 9 illustrate that there is a significant decrease in the concentration of both dyes during irradiation in the presence of all as-synthesized catalysts in comparison to photolysis. Also, these findings reveal that the doped catalysts display excellent photocatalytic degradation performance compared to the undoped ones for TZ and PB dyes. However, the photocatalytic activity clearly increases with the increase in the La content from 5 to 10% which could be related to the presence of the mixed-metal oxides containing MgO, La_2O_3, and $MgAl_2O_4$ that have a relatively smaller band gap than MgO-Al_2O_3 MMO, thus enhancing the visible light absorption of mixed metal oxides. Based on the above, it can be deduced that the optimal content of lanthanum is 10% in our work. This composition is thought to be suitable for the separation of photogenerated e^- and h^+ pairs. Therefore, in the following experiments, the investigation of TZ and PB degradation was mainly focused on MgO-La_2O_3-10% MMO.

Effect of the initial solution pH

pH is a critical factor to understand the surface and charging properties of the catalyst. The effect of pH on the photodegradation of TZ and PB in an aqueous medium was studied at pH of 4.0, 6.0, and 9.0. The values of pH were adjusted using appropriate amounts of HCl or NaOH solutions. The experiments were performed to cover pH at an initial concentration of TZ (20 mg/L) and PB (10 mg/L) over MgO-La_2O_3-10% MMO keeping the same operating conditions, and under UV–visible irradiation (see Figs. 10 and 11). As clarified in the figures, the photocatalytic

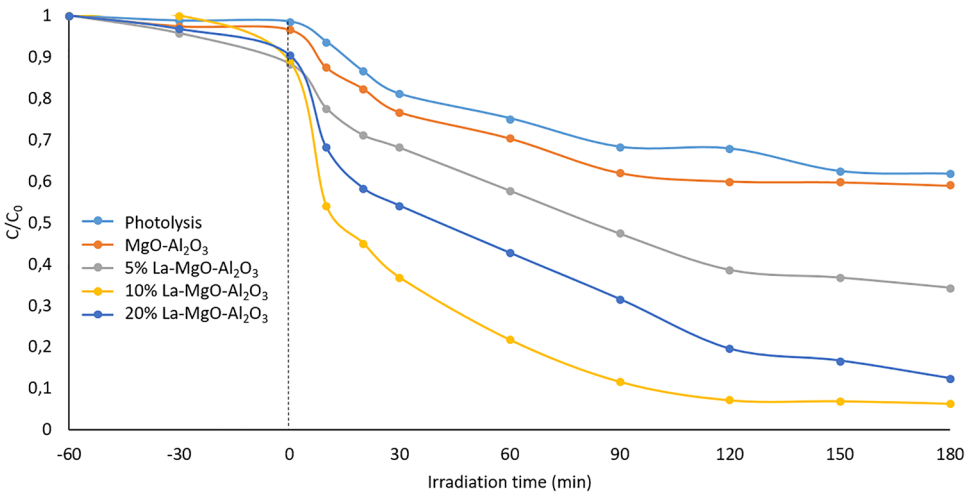

Fig. 9 Adsorption/photocatalytic degradation of PB in the presence of the synthesized samples (PB concentration: 10 mg/L; photocatalyst dosage: 0.3 g/L; irradiation time: 150 min, and pH ~ 4.05)

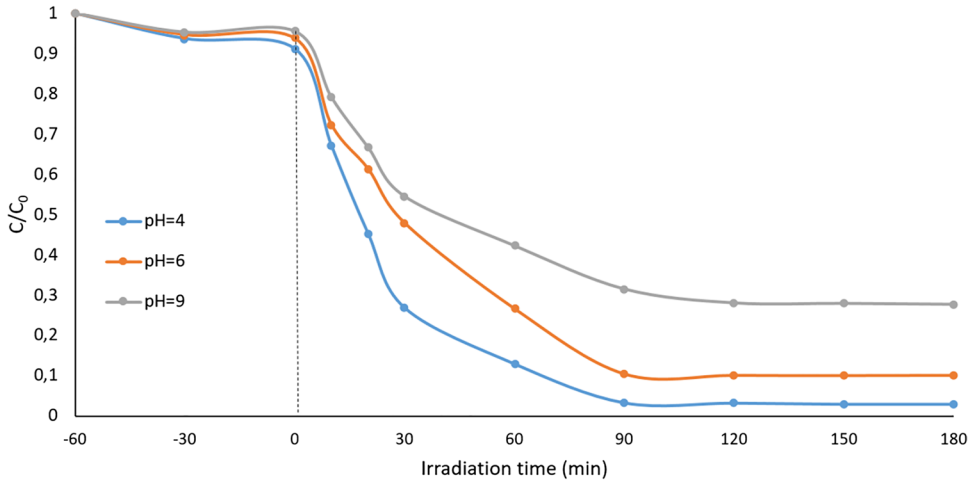

Fig. 10 Effect of the initial solution pH on the photocatalytic degradation of TZ (TZ concentration: 20 mg/L; photocatalyst dosage: 0.3 g/L, and irradiation time: 150 min)

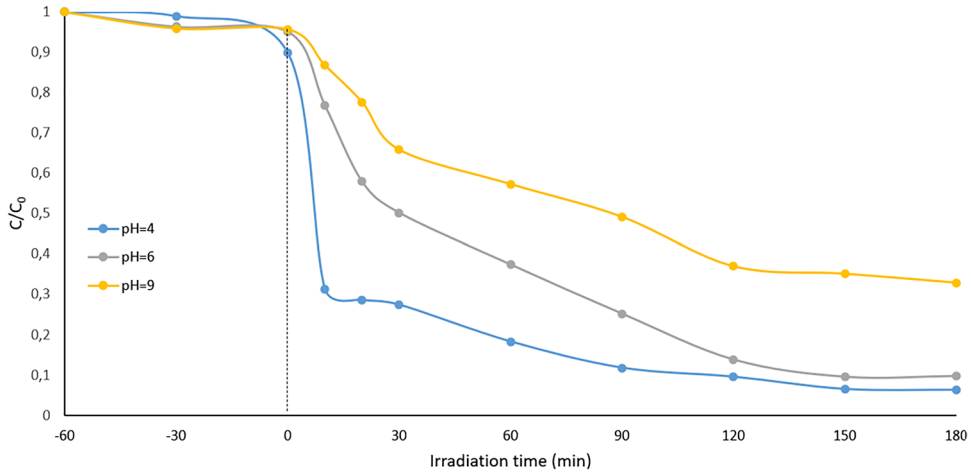

Fig. 11 Effect of the initial solution pH on the photocatalytic degradation of PB (PB concentration: 10 mg/L; photocatalyst dosage: 0.3 g/L, and irradiation time: 150 min)

performance was enhanced at pH of 4 and was decreased significantly at pH 9.0 for both dyes. The adsorption and thus degradation of the dye appear to be selected at a pH lower than the zero-point charge pH (pH_{zpc}), i.e., 7.51 for 10% La-MgO-Al_2O_3-MMO. Generally, the pH of point of zero charge (pH_{pzc}) is an important property of the as-prepared material surface because it affects its ability to adsorb anionic or cationic compounds when they are dispersed into an aqueous solution. When the pH is below the pH_{pzc} value, the solid surface become protonated, and an anionic molecule could be adsorbed. Considering that TZ and PB are anionic dyes, the electrostatic aspects of the process can be discussed. In this regard, the effect of the electrostatic interaction of PB and TZ dyes can be analyzed in terms of their charges with the pH_{ZPC} of the catalysts. The pH_{ZPC} value of the catalysts MgO-La_2O_3-10% MMO is 7.51. Therefore, at pH > 7.51 the surface acquires a negative charge, favoring the adsorption of cationic compounds, while at pH < 7.51, the surface of the catalyst acquires a positive charge, favoring the adsorption of anionic molecules.

Since the PB structure occurs as monovalent anions in the pH region studied ($pK_a = 2.78$), the observed behavior could be uniquely caused by the change in photocatalyst properties. The increase in photocatalytic activity observed at pH 4 could be related to the enhanced adsorption of PB onto the photocatalyst, favored by a pH between 3 and 7 (Fig. 12) and a more efficient formation of hydroxyl radicals. On the other hand, the TZ dye can be reformed to a fully anionic form (Na3Tar (S) 3 Na + (aq) + Tar^{3-}), which explains the maximum adsorption at pH = 4 at pH < 7.51. When the pH of the solution increased, OH^- ions increase in the solution; therefore, OH − ions competed effectively with TZ species for adsorption on the surface of the photocatalyst causing a decrease in the dye removal percentage. Therefore, the functional amine group positively charged will react with a positive charge surface of MgO-La_2O_3-10% MMO at pH < 7.51.

The trend of the photocatalytic activity observed at pH of 4.0 could be due to the favorably enhanced adsorption of both TZ and PB on the photocatalyst at pH values

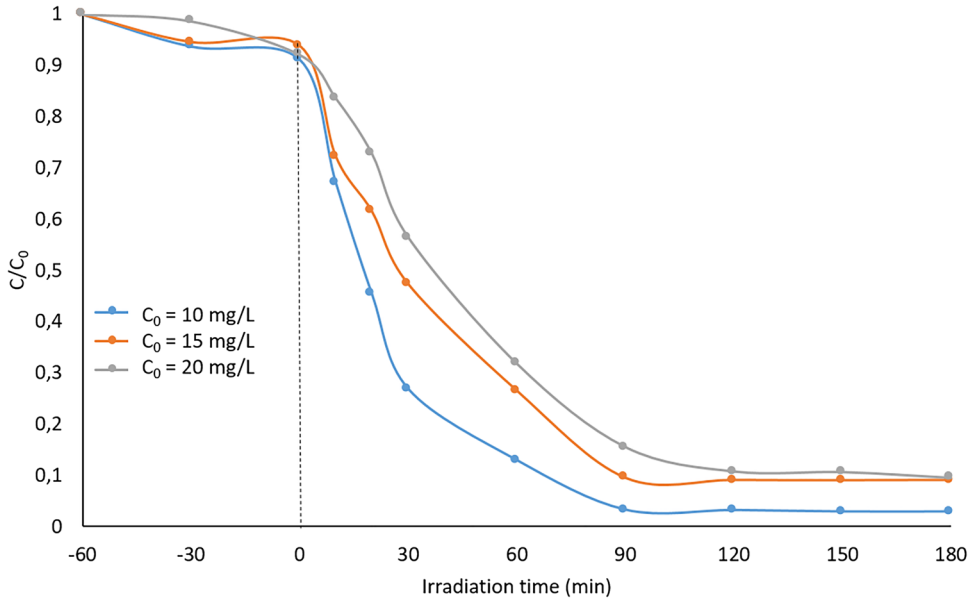

Fig. 12 Effect of initial concentration on the photocatalytic degradation of TZ ([MgO-La_2O_3-10% MMO]$_0$ = 0.3 g/L; irradiation time: 150 min; and pH, ~ 4.08)

between 4 and 7 and the more efficient formation of hydroxyl radicals. In the basic medium (pH = 9.0), the decrease in the degradation efficiency could be attributed to many phenomena simultaneously intervening: the nonfavorable adsorption, and the dissolution of the photocatalysts. Additionally, in an acidic environment, the molecular structure of the dye can be transformed into a quinoid structure, which is unstable and can rapidly be decomposed (Zhang et al. 2018a, b). Nevertheless, a further rise of the pH causes an enhancement of the coulombic repulsion between the negatively charged MgO-La_2O_3-10% MMO surface and the OH species involved in the photocatalytic oxidation mechanism, which implies a decrease in the degradation efficiency.

Effect of the initial concentration of TZ

The influence of the initial dye concentration on its degradation has been investigated with varying concentrations of both dye from 10 to 20 mg/L, keeping the initial solution pH set at 4.08 and the optimum catalyst dose of 0.3 g/L (see Figs. 12 and 13). It is found that the degradation efficiency of the sample has been increased initially for dye concentrations up to 20 mg/L for TZ, whereas the efficiency of the degradation of PB tends to decrease with the increase in the initial concentration above 10 mg/L. As a result, a lower initial dye concentration could improve dye removal efficiency. This might be explained by the fact that as the initial dye concentration was increased, more dye molecules

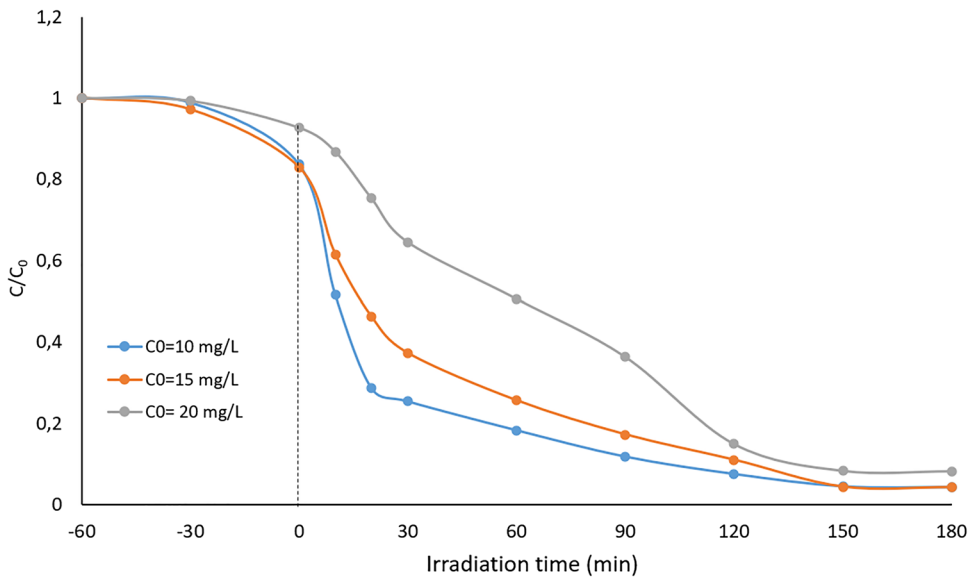

Fig. 13 Effect of initial concentration on the photocatalytic degradation of PB ([MgO-La_2O_3-10% MMO]$_0$ = 0.3 g/L; irradiation time: 150 min; and pH ~ 4.08)

were adsorbed on the photocatalyst surface. The adsorption of O_2 and OH^- on the photocatalyst was decreased, as many active sites were filled by the dye molecules, resulting in a reduction of radical regeneration. Furthermore, photons were inhibited before presenting on the surface of the photocatalyst, resulting in a decrease in photon adsorption by the photocatalyst.

Effect of the photocatalyst dose

Optimal catalyst loading increases the rate of electron/hole pair generation and thus the formation of $OH^{\cdot}$ radicals for water treatment. Therefore, the effect of catalyst dosage on the degradation efficiency was studied by varying the amount of the best photocatalyst (MgO-La_2O_3-10% MMO) in the range of 0.1–0.7 g/L by keeping the concentration of TZ and PB dyes at 20 and 10 mg/L, respectively (see Fig. 14). After 150 min of UV–visible irradiation, the photocatalytic degradation efficiency (%) was evaluated. As can be seen, the photocatalyst amount of 0.3 g/L exhibited the best efficiency for the degradation of TZ and PB, and then a slight decrease in the degradation efficiency occurred with the rise of the catalyst dose.

As the amount of photocatalyst increases, more and more active sites are created on the surface of the photocatalyst, which leads to an increase in the formation of hydroxyl radicals. An increased amount of photocatalysts has a negative effect because aggregation of catalyst particles has a screening effect that prevents photons from reaching the inner catalyst surface.

However, an excessive dose of the photocatalyst decreases light penetration and scattering via the protective effect of the suspended particles and thus reduces the rate of photodegradation.

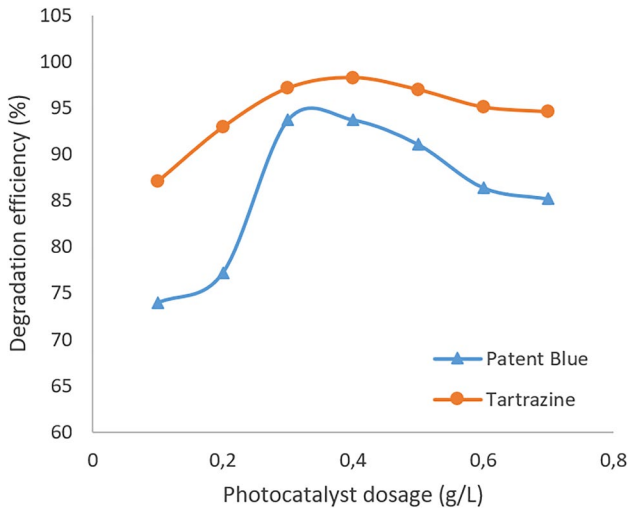

Fig. 14 Effect of photocatalyst dose on the photocatalytic degradation of TZ (20 mg/L) and PB (10 mg/L); 150 min irradiation time and pH ~ 4.05

Efficiency of the regenerated photocatalyst

The reusability of the photocatalyst is crucially important for industrial application due to the cost associated with the synthesis of the catalyst. Therefore, it is important to study the repeating stability of the prepared catalysts. The catalyst was utilized multiple times to demonstrate its efficiency and cost-effectiveness. The catalyst was separated after each dye degradation experiment, washed with distilled water, dried at 100 °C for 24 h, and reused for further studies.

As seen in Fig. 15, the photocatalytic activity of the synthesized photocatalyst was nearly constant for three times cycling for both dyes. The MgO-La_2O_3-10% MMO reveals a high photostability and denotes excellent reusability in these experiments, with small deactivation, which can be attributed to the residual dye adsorbed on the surface of the photocatalyst. The findings suggest that MgO-La_2O_3-10% MMO may have potential application in the environmental remediation issues as stable and effective material.

Analysis of response surface methodology for the TZ and PB photodegradation

The influence of different parameters on the degradation process efficiency of TZ and PB was investigated by Design Expert 11 software, and the experiments were planned through the CCD to optimize the main operating parameters in order to achieve a maximum photodegradation rate of both dyes in aqueous solutions. The CCD matrix and experimental results obtained in the photocatalytic degradation runs are shown in Table 5.

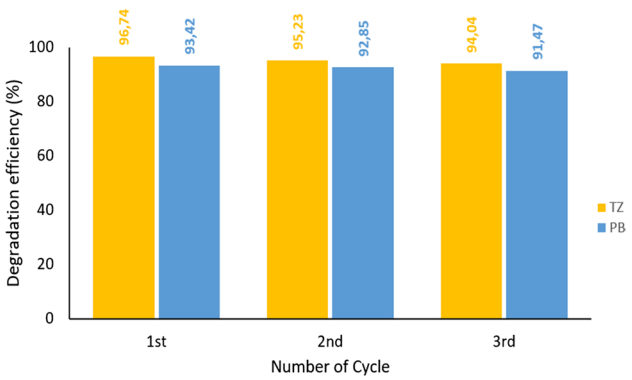

Fig. 15 Photocatalytic degradation of TZ and PB over three cycles of regeneration of the MgO-La_2O_3-10% MMO photocatalyst (TZ concentration: 20 mg/L; PB concentration: 10 mg/L; $[\text{MgO-La}_2\text{O}_3\text{-10\% MMO}]_0 = 0.3$ g/L; and pH ~ 4.05)

Table 5 The 4-factor central composite design matrix and the value of response function (degradation efficiency (%))

Run	Initial dye concentration (mg/L)	pH	Photocatalyst dosage (g/L)	Reaction time (min)	Degradation efficiency (%)			
					Observed		Predicted	
					TZ	PB	TZ	PB
1	15	5	0.4	130	95.413	94.629	95.45	94.27
2	15	7	0.4	130	94.322	93.182	94.45	93.22
3	20	4	0.3	150	97.257	93.642	97.67	94.34
4	15	3	0.4	130	97.174	96.457	96.44	96.17
5	10	6	0.3	110	96.223	92.657	96.02	93.35
6	20	6	0.5	150	93.457	92.403	93.88	92.67
7	20	4	0.5	110	93.915	94.485	94.03	94.4
8	10	4	0.5	150	95.128	94.175	95.07	94.63
9	20	6	0.3	150	97.175	94.402	96.68	94.45
10	15	5	0.4	130	95	93.772	95.45	94.27
11	5	5	0.4	130	95.214	99.573	95.64	99.87
12	15	5	0.6	130	92.481	92.914	92.65	92.58
13	20	6	0.5	110	93.221	90.28	93.03	91.18
14	15	5	0.4	130	94.645	94.798	95.45	94.27
15	10	6	0.5	150	94.245	95.011	94.07	95.1
16	15	5	0.4	90	94.364	91.222	94.6	91.24
17	15	5	0.4	130	95.525	93.646	95.45	94.27
18	10	4	0.3	110	96.741	97.117	97.01	96.61
19	20	6	0.3	110	95.662	94.885	95.83	94.19
20	15	5	0.4	130	95.525	94.788	95.45	94.27
21	10	6	0.3	150	96.665	93.147	96.87	92.99
22	25	5	0.4	130	95.348	98.987	95.26	98.44
23	15	5	0.4	170	97.247	89.117	96.3	88.84
24	15	5	0.2	130	98.456	93.598	98.24	93.68
25	20	4	0.5	150	94.217	92.55	94.88	92.36
26	10	4	0.5	110	94.785	96.842	94.22	97.29
27	15	5	0.4	130	96.328	93.98	95.45	94.27
28	10	4	0.3	150	97.248	93.122	97.86	92.72
29	10	6	0.5	110	93.437	95.17	93.23	94.23
30	20	4	0.3	110	97	97.197	96.82	97.61

The second-order polynomial response equation (Eq. (4)) was employed to correlate the dependent and independent variables:

$$Y = \beta_0 + \sum_{i=1}^{k} \beta_i x_i + \sum_{i=1}^{k} \beta_{ii} x_i^2 + \sum_{i<j} \beta_{ij} x_i x_j + \varepsilon \tag{4}$$

In this expression, β_0 represents the interception term, x_i and x_j are the variable parameters of i and j with number k, and β_i, β_{ii}, andβ_{ij} represent the linear, quadratic, and interaction parameter coefficients, respectively. Lastly, the term ε indicates the random error.

Based on these outcomes, an empirical relationship between the response and independent parameters established and expressed by the proposed second-order polynomial equations (Eqs. (6) and (7)) for TZ (Y_1) and PB (Y_2), respectively.

$$\begin{aligned} Y1 = {} & 95.41 - 0.0958X_1 - 0.4962X_2 - 1.4X_3 \\ & + 0.4239X_4 + 0.0286X_1X_2 - 0.1876X_1X_3 \\ & + 0.0130X_1X_4 - 0.0728X_2X_3 + 0.0994X_2X_4 \\ & - 0.0644X_3X_4 - 0.0608X_1^2 + 0.0560X_2^2 \\ & - 0.0139X_3^2 + 0.0703X_4^2 \end{aligned} \tag{5}$$

$$Y2 = 94.27 - 0.3570X_1 - 0.7385X_2 - 0.2759X_3 + 0.5996X_4 - 0.0396X_1X_2 - 0.9727X_1X_3 + 0.1551X_1X_4 + 0.0499X_2X_3 + 0.8827X_2X_4 + 0.3066X_3X_4 + 1.22X_1^2 + 0.1063X_2^2 - 0.2846X_3^2 - 1.06X_4^2 \quad (6)$$

Photocatalytic efficiencies ($R(\%)$) have been predicted as shown in Eqs. (5) and (6) and presented in Table 3. These results indicated good agreements between the experimental and predicted values of degradation efficiency. The predicted values were found to match the experimental values with a good fit with $R^2 = 0.9327$ and $R^2 = 0.9574$ for TZ and PB, respectively.

This suggests that 93.27% and 95.74% of the variations for TZ and PB removal are explained by the independent variables, and this also signifies that the model does not explain only about remaining 6.73% and 4.26% of variation.

The significance and adequacy of the quadratic RSM with regard to the interactions of the independent parameters were explained by analysis of variance (ANOVA), and the obtained results are displayed in Table 6. Degrees of freedom (D_f), sum of squares, and mean squares were determined. Similarly, the F and p values were utilized to exhibit the significance of the quadratic model terms. The terms with high F-values and p-values less than 0.05 were considered significant, and those with low F-values and p-values more than 0.05 were considered insignificant. The F-values obtained for TZ and PB of 14.85 and 24.06, respectively, are clearly greater than the tabulated F (2.352 at 95% significance) confirming the adequacy of the model for processing the data. On the other hand, the proposed quadratic model can effectively analyze 95% of the data. Moreover, the F-value for the lack-of-fit (LOF) term for TZ and PB were 0.801 and 1.77 which were smaller than the critical F 0.05 = 8.79, confirming the goodness of the model from a statistical point of view. A high LOF indicates that the adjusted model is unable to fit the data adequately, whereas a nonsignificant term indicates the variation in the data according to the fitted model. Another evidence for the quality of the applied model is the regression coefficient values presented in table that were obtained from the ANOVA. In this instance, the multiple coefficients of determination R^2, the adjusted one, and the predicted one are close to the unity (1), confirming the accuracy of the suggested models and their efficiency in processing the data. Once the R^2 value approaches the adjusted R^2 value, it means that the proposed models contain the significant parameters and that all the selected parameters have an essential role in the response variable. Here, the adjusted R^2 values for TZ and PB (0.8699; 0.9176) were very close to the corresponding R^2 value (0.9327 and 0.9574 for TZ and PB, respectively).

In an excellent model in RSM, to obtain a good design space, the value of the adequate precision (or S/N) must be higher than 4 (Karimifard and Moghaddam 2018). In this study, the adequate precision was 14.89 and 23.96 for TZ and PB, respectively. Also, the coefficient of variance (C.V. %) value for both dyes (0.5558 and 0.69 for TZ and PB,

Table 6 Analysis of variance (ANOVA) for fit of degradation efficiency from central composite design

Source of variation	Sum of square		D_f		Mean square		F-value		P-value	
	TZ	PB	TZ	PB	TZ	PB	TZ	PB	TZ	PB
Model	58.51	142.55	14	14	4.18	10.18	14.85	24.06	< 0.0001	< 0.0001
X_1	0.2204	3.06	1	1	0.2204	3.06	0.7832	7.23	0.3901	0.0168
X_2	5.91	13.09	1	1	5.91	13.09	21	30.93	0.0004	< 0.0001
X_3	46.81	1.83	1	1	46.81	1.83	166.31	4.32	< 0.0001	0.0554
X_4	4.31	8.63	1	1	4.31	8.63	15.33	20.39	0.0014	0.0004
X_1X_2	0.0131	0.025	1	1	0.0131	0.025	0.0466	0.0592	0.832	0.8111
X_1X_3	0.5633	15.14	1	1	0.5633	15.14	2	35.76	0.1776	< 0.0001
X_1X_4	0.0027	0.3847	1	1	0.0027	0.3847	0.0096	0.9089	0.9232	0.3555
X_2X_3	0.0847	0.0399	1	1	0.0847	0.0399	0.3009	0.0943	0.5914	0.763
X_2X_4	0.158	12.47	1	1	0.158	12.47	0.5614	29.45	0.4653	< 0.0001
X_3X_4	0.0663	1.5	1	1	0.0663	1.5	0.2356	3.55	0.6344	0.079
X_1^2	0.1014	40.92	1	1	0.1014	40.92	0.3602	96.67	0.5574	< 0.0001
X_2^2	0.0859	0.3097	1	1	0.0859	0.3097	0.3052	0.7317	0.5888	0.4058
X_3^2	0.0053	2.22	1	1	0.0053	2.22	0.0189	5.25	0.8926	0.0369
X_4^2	0.1357	30.6	1	1	0.1357	30.6	0.4821	72.29	0.4981	< 0.0001
Residual	4.22	6.35	15	15	0.2814	0.4233				
Lack of fit	2.6	4.95	10	10	0.2599	0.4952	0.801	1.77	0.6433	0.2741
Pure error	1.62	1.4	5	5	0.3245	0.2795				
Cor total	62.73	148.9	29	29						

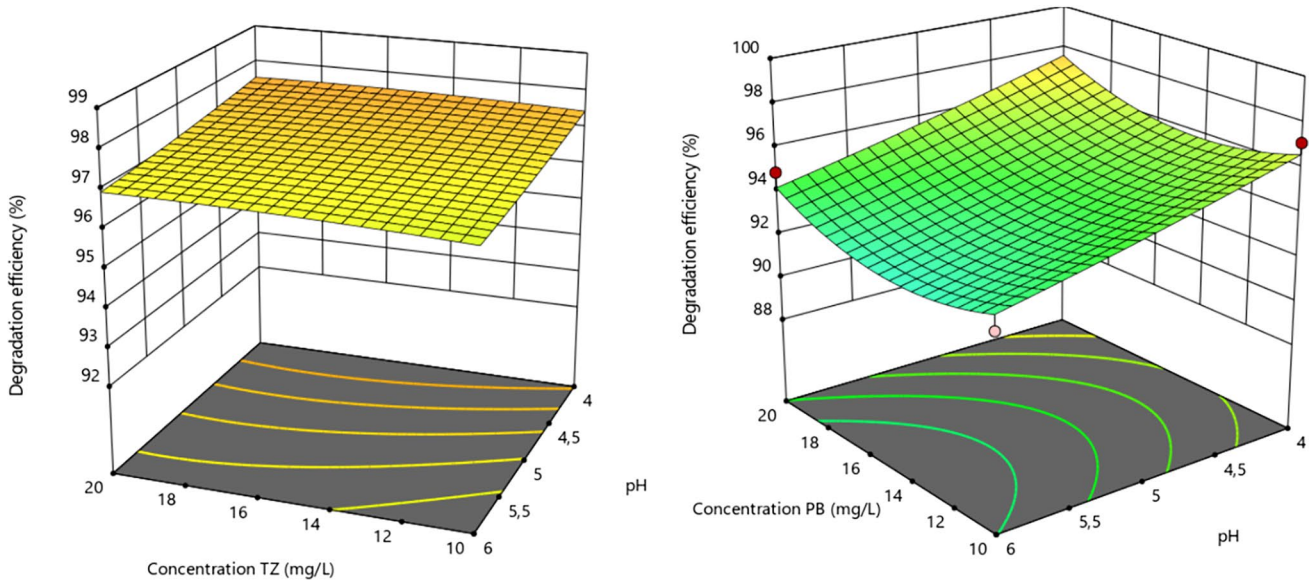

Fig. 16 The response surface and contour plots of photocatalytic degradation efficiency (%) as the function of pH and initial dye concentration (mg/L) of TZ and PB

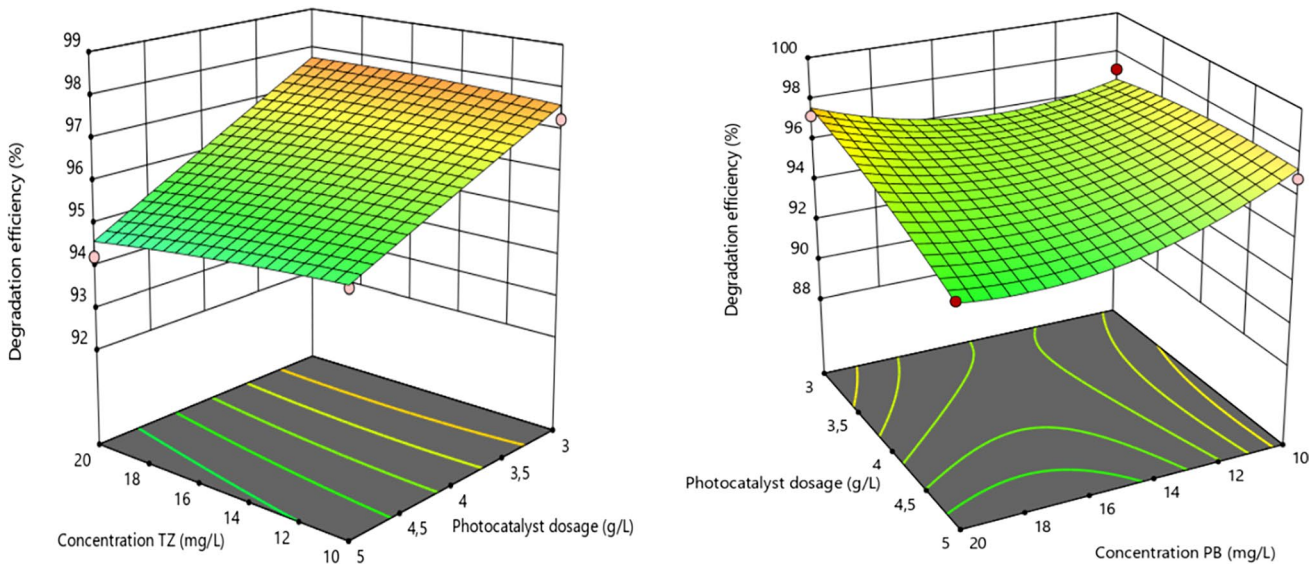

Fig. 17 The response surface and contour plots of photocatalytic degradation efficiency (%) as the function of photocatalyst dosage (g/L) and initial dye concentration (mg/L) of TZ and PB

respectively) were very low which indicates the plausibility and reproducibility of the model. Thus, the proposed model can be applied to predict the degradation efficiency of TZ and PB by MgO-La_2O_3 MMO heterostructured catalysts.

Another evidence for the validity of the applied model in the RSM approach is influencing plots which are presented in Fig. 18. As can be seen from the figure, the predicted data were randomly distributed around their experimental values and no tendency was observed for TZ and PB.

3D response surface plots are a useful tool for visualizing the depiction of coexistent interaction effects between binary influence test variables. The response surface plots for TZ and PB degradation obtained in this study from Eqs. (5) and (6) are displayed in Figs. 16, 17, and 18. Responses were represented as a function of two factors, with the other variable being constant. The findings proved that the interactions of the four mentioned parameters were significant. Figure 16 illustrates the effect of

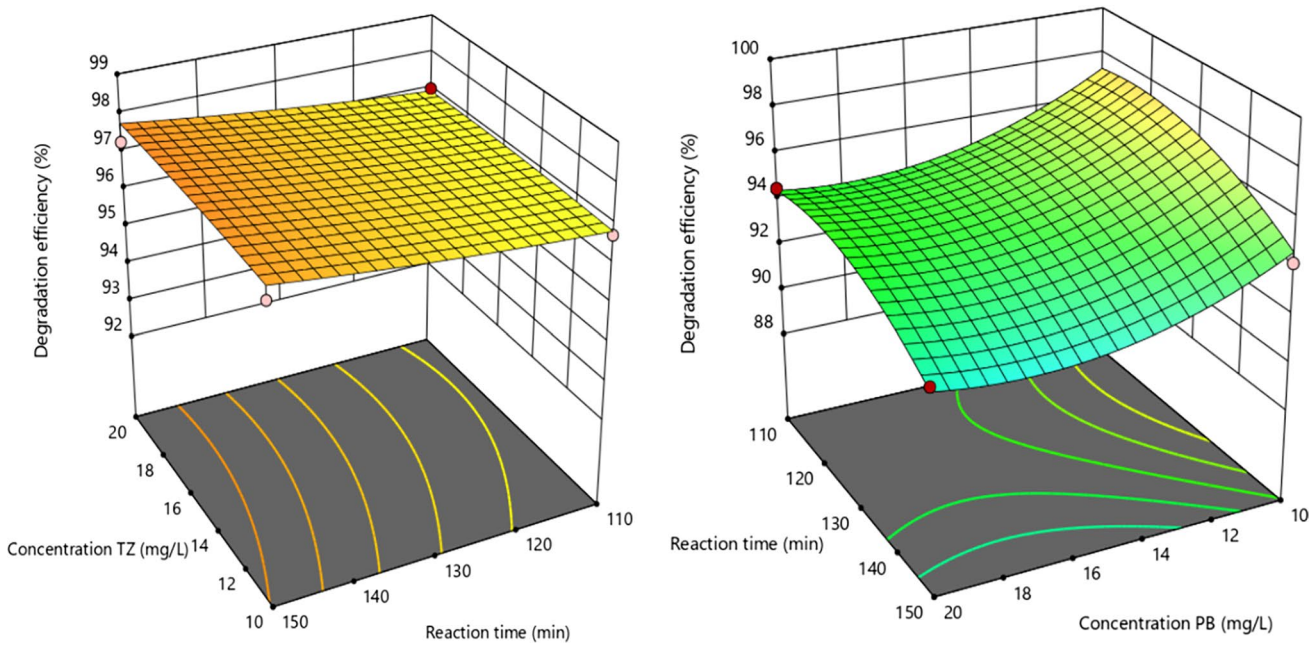

Fig. 18 The response surface and contour plots of photocatalytic degradation efficiency (%) as the function of reaction time (min) and initial dye concentration (mg/L) of TZ and PB

pH and initial dye concentration on photocatalytic degradation efficiency of TZ and PB for an initial dye concentration of 0.3 g/L and reaction time of 150 min. As it is obvious from the figure, the best response was obtained at a pH of about 4 through the whole range of the initial dye concentration (10–20 mg/L). This can be attributed to various factors. As mentioned in "Effect of the initial solution pH," the pH_{pzc} of the catalyst was estimated at 7.8. At $pH_s < 7.8$, the protonated dye molecules can be repelled by the positively charged surface of the catalyst. At pH greater than 7.8, the catalyst surface has a negative charge, which creates an attractive force between it and both dyes, which have been deprotonated and behave like hydrophobic molecules (Mossavi et al. 2022).

The interaction effects between the dose of the catalyst and the initial dye concentration are displayed in Fig. 17. As it is obvious. the degradation efficiency was diminished by raising the dose of the catalyst, whereas the best degradation efficiency was achieved in the dose of the catalyst around 3 g/L. When the pH and reaction time are constant, the active sites on the photocatalyst surface diminish with the enhancement of the dyes concentration, which reduces the degradation efficiency.

The interaction effects between the initial dye concentration and reaction time in Fig. 18 show the best degradation efficiency of TZ in the moderate reaction time (about 150 min) through the used range for the initial concentration of TZ. At the same time, Fig. 20 shows that at a moderate concentration of PB (10 mg/L), the best degradation of PB was obtained through the whole range of the reaction time.

In summary, the optimal RSM run includes pH 4, catalyst dosage 0.3 g/L, initial concentration of TZ 20 mg/L, and reaction time 150 min for the maximum degradation efficiency of TZ (97.31%). On the other hand, the optimum values of the factors for the maximum degradation efficiency of PB were 10 mg/L, 4, 0.3 g/L, and 150 min for initial dyes concentration (X_1), pH (X_2), photocatalyst dose (X_3), and reaction time (X_4), respectively (94.46%).

The GBR model performance

Based on the same data selection as employed in the RSM model, GBR analysis was conducted to establish a nonlinear algorithm for predicting the photocatalytic degradation of the tartrazine and patent blue. The initial dye concentration, pH, photocatalyst dose, and reaction time were considered as input data for the model, and degradation efficiency was described as output. The experimental datasets were randomly subdivided into three subsets, including the training, testing, and validation (80%, 10%, and 10% of the set points were applied, respectively) in the aim of predicting the capabilities of the GBR for the unobserved data set. The mean square error

(MSE) and regression analysis coefficient (R^2) were used to evaluate its performance.

It is worthy to note that before starting the training of the GBR model, novel nonlinear features were added consisting of polynomial combinations (degree 3) of the input data in order to improve the predictive quality of the model. Subsequently, the influence factor data as inputs were first normalized by employing Eq. 7 before building the machine learning model.

$$x_i^* = \frac{x_i - \mu}{\sigma} \tag{7}$$

where x_i^* and x_i correspond to the normalized and original values of input parameters, respectively; μ and σ represent the mean value and standard deviation for each parameter, respectively. The procedure for regularizing the GBR algorithm generally consists of optimizing two parameters that are max_depth and allowing to set it as n_estimators, which corresponds to the number of regression trees constructed based on a bootstrap stage that will be performed, and max_depth is the limit of the number of nodes in the tree. GBR is effective enough to avoid overfitting; therefore, a high number generally gives better performance.

The GBR model was fitted with variable values for n_estimators (100–5000). The findings suggest that the optimal tuning parameters for the GBR model of TZ and PB are achieved based on the n_{tree} of 750 and 700, respectively. The max_depth parameter determines the maximum depth of each tree. The default values for max_depth are 18 for TZ and 12 for PB.

Regarding the training data set, the coefficient of determination R^2 values of 0.9882 and 0.9868 for TZ and PB, respectively, and the MSE values for TZ and PB (0.0228, 0.0629), which were very low, for the GBR model are obtained. This implies that 98.82% and 98.68% of the variations for the photocatalytic decolorization of TZ and PB are attributed to the independent variables, and this also implies that the model does not explain only about 1.18% and 1.32% of the variation, which confirms the high accuracy of the GBR model for modeling and prediction of the dye elimination.

Possible photocatalytic mechanism

The photocatalytic degradation performance depends on many factors including the band gap energy and electron–hole pair recombination rate of the photocatalyst. The photocatalysts elaborated in this research are mainly based on the modification of active MgO by uniform distribution of La through the LDH structure. In general, both MgO and La_2O_3 are irradiated under UV visible as results in the propagation of an electron from valence band (VB) to the conduction band (CB) and the generation of hole or electron deficiency in the VB as illustrated in Fig. 19.

According to the mechanism described above, the energy band diagram of a semiconductor photocatalyst illustrates the role of light absorption and the oxidative and reductive capabilities of photogenerated charge carriers, and ultimately determines photocatalytic activity. The electron–hole charges are photogenerated through an excitation process on the surface of MgO/La_2O_3 by ultraviolet–visible light. According to the literature, the valence band potential of La_2O_3 (5.2 eV) is more negative when compared with MgO (7.8 eV) (Kumari et al. 2019; Pathak et al. 2016). In fact, based on the results of the UV–vis diffuse reflectance spectroscopy, the combination of the two catalysts resulted in the formation of a smaller band gap (3.05 eV), thereby enhancing the photocatalytic activity in the visible light zone. As a result, the MgO-La_2O_3-MMO needs less energy to form electron–hole pairs, allowing for more photons to be used, leading to improved photocatalytic activity. A large number of photogenerated charges accumulated on the surface of catalyst permitted the photodegradation of dye based on the following reactions:

$$MgO/La_2O_3 + hv \rightarrow h^+_{VB} + e^-_{CB} \tag{8}$$

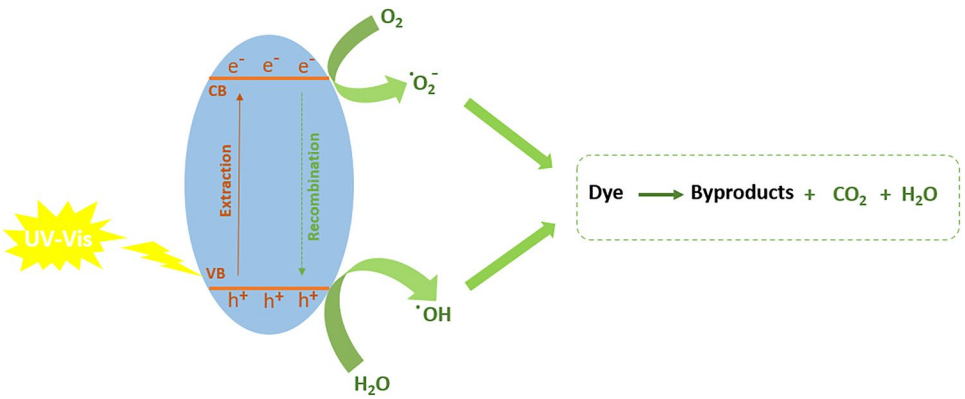

Fig. 19 Possible photocatalytic mechanism for dye degradation

Table 7 Comparison of photocatalytic performances of MgO-La_2O_3-MMO for the degradation of TZ and PB in aqueous medium with other catalysts reported in the literatures

LDH	Light source	Dye	Initial concentration (mg/L)	Time (min)	Efficiency	Ref
TiO_2/g-C_3N_4	Sunlight	Tartrazine	20	60	93	Cao et al. (2022)
Ag-doped TiO_2	Vis	Tartrazine	10	180	87	Ratshiedana et al. (2021a, b)
TiHAp	UV	Patent Blue	20	24 h	~100	Bekkali et al. (2016)
MgP	UV	Patent Blue	15	70	99,5	Sadiq et al. (2021)
(Ce, Ag)/ZnO	Sunlight	Tartrazine	10	90	99	Bouarroudj et al. (2021)
ZnO	UV	Tartrazine	10	70	100	Tu and Tuan (2018)
Cu-mpg-C_3N_4	UV	Tartrazine	10	250	81,9	Zhang et al. (2018a, b)
TiO_2	UV	Tartrazine	15	240	83	Souza et al. (2021)
Zn-Co-MMO	UV–vis	Tartrazine	20	240	75	Abd-Ellatif et al. (2022)
TiO_2/GO	Sunlight	Tartrazine	40	240	63	Ramos et al. (2020)
MRGT50	Vis	Tartrazine	50	210	96	Nada et al. (2018)
MgO-La_2O_3-MMO	UV–vis	Tartrazine	20	150	97.25	**This work**
MgO-La_2O_3-MMO	UV–vis	Patent Blue	10	150	93.64	**This work**

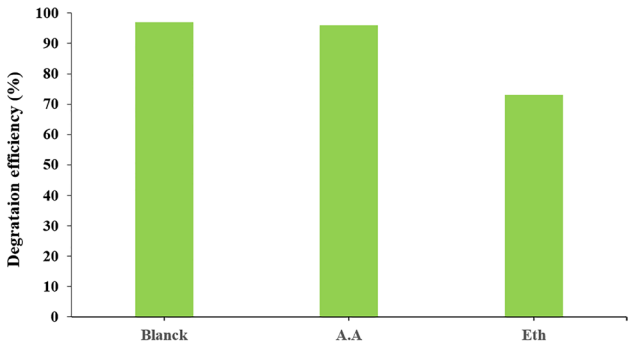

Fig. 20 Effect of scavenger on degradation of TZ

$$\text{Reductionprocesses}: e^- + O_2 \rightarrow O_2^{\cdot -} \quad (9)$$

$$O_2^{\cdot -} + H^+ \rightarrow \text{HOO}^{\cdot} \quad (10)$$

$$\text{HOO} + {}^{\cdot}\text{HOO}^{\cdot} \rightarrow H_2O_2 + O_2 \quad (11)$$

$$H_2O_2 + O_2^{\cdot -} \rightarrow OH^- + OH^{\cdot} + O_2 \quad (12)$$

$$H_2O_2 + h \rightarrow OH^{\cdot} \quad (13)$$

$$\text{Oxidationprocesses}: H_2O + La_2O_3(h^+) \rightarrow H^+ + OH^{\cdot} \quad (14)$$

$$OH^- + La_2O_3(h^+) \rightarrow OH^{\cdot} \quad (15)$$

$$\text{Dye} + HO^{\cdot} \rightarrow \text{Dye}(HO^{\cdot}) \rightarrow \text{Intermediates} + HO^{\cdot} \rightarrow CO_2 + H_2O \quad (16)$$

In Table 7, the comparison of the proposed MgO-La_2O_3-MMO catalyst with other reported materials for TZ and PB degradation reported in the literature under simulated solar light, UV, visible, or both UV and Vis irradiation was summed up. The proposed material exhibited enhanced catalytic performance, which achieved a higher degradation efficiency in a shorter time.

Effect of dosage and scavenger's trapping

To understand the reactive oxygen species (ROS) responsible for the degradation, the scavenging experiments were performed using different scavengers, namely, ascorbic acid (AA, scavenger for $O_2^{\cdot -}$) and ethanol (Eth, scavenger for ·OH radicals) as reported in the literature (Ratshiedana et al. 2021a, b; Elangovan et al. 2021). The scavenger's ethanol (1 mmol) and acid ascorbic (10 mmol) were added to a series of 100 mL of tartrazine solution with an initial concentration of 20 mg/L prior to UV–vis irradiation and with the inclusion of the catalyst.

As illustrated in Fig. 20, the highest photodegradation was observed in the absence of the scavengers. When AA was introduced into the solution, the photocatalytic activity was slightly decreased, which implies a small contribution superoxide radical. Nevertheless, the addition of Eth caused a significant reduction in photodegradation, suggesting that the hydroxyl radical is the dominant ROS species.

Conclusion

In the present paper, a series of MgAl-%La-CO_3 LDHs with various contents of La (5, 10, and 20 wt%) have been successfully prepared by the co-precipitation process under constant pH and employed as precursors for the synthesis of mixed oxides MgO-La_2O_3 MMO. The synthesized heterostructure catalysts were characterized employing various physicochemical techniques including XRD, SEM/EDX, FTIR, TGA, and ICP-MS. The incorporation of La into the lattice was confirmed through FTIR and Raman characterization. The MgAl-%La-CO_3 LDH sample exhibits a typical hydrotalcite structure, whose crystallinity decreases as the amount of La increases as a result of partial Al substitution. The photocatalytic performance of the as-synthesized was assessed for the degradation of textile dyes, TZ, and PB as a model of organic pollutants in an aqueous medium under UV–visible irradiation. The effect of the La^{3+}, initial concentration of dye, and initial pH was investigated. It was found that the presence of La absolutely improved the photocatalytic activity of the MgAl-MMO for the degradation of both studied pollutants under UV–visible irradiation. All catalysts exhibited improved effects for both dyes, but the best performance was reached with the MgO-La_2O_3-10% MMO catalyst. The second interest of this study was to assess the performance of two AI techniques, namely, RSM and GBR, in predicting the removal of two model pollutants and estimating the values of new observations. The MSE and R^2 statistical criteria were explored to evaluate the predictive performance of the two AI approaches. The GBR model developed from the reduced experimental data performed significantly better in the validation experiments, meaning that this model was able to capture the nonlinearities in the experimental data more effectively than the RSM technique, with a regression coefficient greater than 98% for the photocatalytic removal efficiency of both dyes. From this study, it can be seen that this photocatalyst presents an exceptional performance to be applied for the degradation of recalcitrant organic pollutants such as dyes. Also, this paper can be considered as a stimulus to encourage and inspire other scientists to conceive and optimize technologies such as the photodegradation process for efficient wastewater treatment based on AI techniques.

Author contribution N. Taoufik: conceptualization, investigation, formal analysis, writing — original draft preparation. F. Z. Janani: formal analysis, writing — original draft. H. Khiar: formal analysis, writing — original draft. M. Sadiq: writing — original draft. M. Abdennouri: analyzed and interpreted the data; writing, review, and editing; data curation. M. Sillanpää, analyzed and interpreted the data; writing, review, and editing; data curation. M. Achak: writing — original draft. N. Barka: supervision, analyzed and interpreted the data; data curation; writing, review, and editing; conceptualization; validation.

Availability of data and materials All data and materials generated or analyzed during this study were included in this published article.

Declarations

Ethics approval and consent to participate Not applicable.

Consent for publication Not applicable.

Competing interests The authors declare no competing interests.

References

Abd-Ellatif WR, Mahmoud NG, Hashem AA, El-Aiashy MK, Ezzo EM, Mahmoud SA (2022) Efficient photodegradation of E124 dye using two-dimensional Zn-Co LDH: kinetic and thermodynamic studies. Environ Technol Innovation 27:102393. https://doi.org/10.1016/j.eti.2022.102393

Abdi J, Sisi AJ, Hadipoor M (2022) Khatae A (2022) State of the art on the ultrasonic-assisted removal of environmental pollutants using metal-organic frameworks. J Hazard Mater 424:127558. https://doi.org/10.1016/j.jhazmat.2021.127558

Ai Z, Liu C, Zhang Q, Qu J, Li Z, He X (2018) Adding ZnO and SiO_2 to scatter the agglomeration of mechanochemically prepared Zn-Al LDH precursor and promote its adsorption toward Methyl Orange. J Alloys Compd 763:342–348. https://doi.org/10.1016/j.jallcom.2018.05.201

Ali MA, Mubarak MF, Keshawy M, Zayed MA, Ataalla M (2022) Adsorption of tartrazine anionic dye by novel fixed bed core-shell-polystyrene divinylbenzene/magnetite nanocomposite. Alex Eng J 61:1335–1352. https://doi.org/10.1016/j.aej.2021.06.016

An X, Gao C, Liao J, Wu X, Xie X (2015) Synthesis of mesoporous N-doped TiO_2/ZnAl-layered double oxides nanocomposite for efficient photodegradation of methyl orange. Mater Sci Semicond Process 34:162–169. https://doi.org/10.1016/j.mssp.2015.02.003

Baliarsingh N, Parida KM, Pradhan GC (2014) Effects of Co, Ni, Cu, and Zn on photophysical and photocatalytic properties of carbonate intercalated MII/Cr LDHs for enhanced photodegradation of methyl orange. Ind Eng Chem Res 53:3834–3841. https://doi.org/10.1021/ie403769b

Balthazard-Accou K, Emmanuel E, Agnamey P, Raccurt C (2019) Pollution of water resources and environmental impacts in urban areas of developing countries: case of the city of Les cayes (Haiti). Environmental Health - Management and Prevention Practices, IntechOpen. https://doi.org/10.5772/intechopen.86951

Banu V, Mohamed H, Arunprasath R (2019) Biological treatment of azo dyes on effluent by Neurospora sp isolated and adopted from dye contaminated site. J Text Inst 111:1–7. https://doi.org/10.1080/00405000.2019.1690917

Barka N, Qourzal S, Assabbane A, Nounah A, Ait-Ichou Y (2011) Photocatalytic degradation of patent blue V by supported TiO_2: kinetics, mineralization, and reaction pathway. Chem Eng Commun 198:10. https://doi.org/10.1080/00986445.2010.525206

Barka N, Bakas I, Qourzal S, Assabbane A, Ait-Ichou Y (2013) Degradation of phenol in water by titanium dioxide photocatalysis. Orient J Chem 29:1055–1060. https://doi.org/10.13005/ojc/290328.

Bekkali CE, Bouyarmane H, Saoiabi S, Karbane ME, Rami A, Saoiabi A, Boujtita M, Laghzizil A (2016) Low-cost composites based on porous titania-apatite surfaces for the removal of patent blue V from water: effect of chemical structure of dye. J Adv Res 7:1009–1017. https://doi.org/10.1016/j.jare.2016.05.001

Bessaha H, Bouraada M, de Menorval LC (2017) Removal of an acid dye from water using calcined and uncalcined ZnAl-r anionic clay.

Water Environ Res 89:783–790. https://doi.org/10.2175/106143017X14902968254809

Bhagat SK, Tiyasha T, Tung TM, Mostafa RR, Yaseen ZM (2020) Manganese (Mn) removal prediction using extreme gradient model. Ecotoxicol Environ Saf 204:111059. https://doi.org/10.1016/j.ecoenv.2020.111059

Bhagat SK, Tung TM, Yaseen ZM (2021) Heavy metal contamination prediction using ensemble model: case study of bay sedimentation. Australia J Hazard Mater 403:123492. https://doi.org/10.1016/j.jhazmat.2020.123492

Bilinska L, Gmurek M (2021) Novel trends in AOPs for textile wastewater treatment. Enhanced dye by-products removal by catalytic and synergistic actions. Water Resour Ind 26:100160. https://doi.org/10.1016/j.wri.2021.100160

Bouarroudj T, Aoudjit L, Djahida L, Zaidi B, Ouraghi M, Zioui D, Mahidine S, Shekhar C, Bachari K (2021) Photodegradation of tartrazine dye favored by natural sunlight on pure and (Ce, Ag) co-doped ZnO catalysts. Water Sci Technol 83:2118–2134. https://doi.org/10.2166/wst.2021.106

Cai PW, Ci SQ, Wu N, Hong Y, Wen ZH (2017) Layered structured CoAl/CdS-LDHs nanocomposites as visible light photocatalyst. Phys Status Solidi A 214:1–7. https://doi.org/10.1002/pssa.201600910

Cao Y, Yuan G, Guo Y, Hu X, Fang G, Wang S (2022) Facile synthesis of TiO_2/g-C_3N_4 nanosheet heterojunctions for efficient photocatalytic degradation of tartrazine under simulated sunlight. Appl Surf Sci 600:154169. https://doi.org/10.1016/j.apsusc.2022.154169

Cocheci L, Lupa L, Olea NST, Muntean C, Negrea P (2020) Sequential use of ionic liquid functionalized Zn-Al layered double hydroxide as adsorbent and photocatalyst. Separ Purif Technol 250:117104. https://doi.org/10.1016/j.seppur.2020.117104

Costa D, Mendonça M, Lopes M, Fernandes AL, Nunes S, Muller S (2020) Patent blue V dye anaphylaxis: a case report and literature review. Braz J Anesthesiol Engl Ed 70:662–666. https://doi.org/10.1016/j.bjane.2020.10.003

El Hanandeh A, Mahdi Z, Imtiaz MS (2021) Modelling of the adsorption of Pb Cu and Ni ions from single and multi-component aqueous solutions by date seed derived biochar: comparison of six machine learning approaches. Environ Res 192:110338. https://doi.org/10.1016/j.envres.2020.110338

Elangovan M, Bharathaiyengar SM, PonnanEttiyappan J (2021) Photocatalytic degradation of diclofenac using TiO_2-CdS heterojunction catalysts under visible light irradiation. Environ Sci Pollut Res 28(18186):18200. https://doi.org/10.1007/s11356-020-11538-w

Elhalil A, Elmoubarki R, Farnane M, Machrouhi A, Mahjoubi FZ, Sadiq M, Qourzal S, Barka N (2018) Photocatalytic degradation of caffeine as a model pharmaceutical pollutant Mg doped ZnO-Al_2O_3 heterostructure. Environ Nanotechnol Monit Manag 10(63–72):7. https://doi.org/10.1016/j.enmm.2018.02.002

Elhalil A, Elmoubarki R, Farnane M, Machrouhi A, Mahjoubi FZ, Sadiq M, Qourzal S, Abdennouri M, Barka N (2019) Novel Ag-ZnO-$La_2O_2CO_3$ photocatalysts derived from the layered double hydroxide structure with excellent photocatalytic performance for the degradation of pharmaceutical compounds. J Sci Adv Mater Devices 4:34–46. https://doi.org/10.1016/j.jsamd.2019.01.002

Elmoubarki R, Mahjoubi FZ, Elhalil A, Tounsadi H, Abdennouri M, Sadiq M, Qourzal S, Zouhri A, Barka N (2017) Ni/Fe and Mg/Fe layered double hydroxides and their calcined derivatives: preparation, characterization and application on textile dyes removal. J Mater Res Technol 6:271–283. https://doi.org/10.1016/j.jmrt.2016.09.007

Elmoubarki R, Boumya W, Mahjoubi FZ, Elhalil A, Sadiq M, Barka N (2021) Ni-Fe-SDS and Ni-Fe-SO_4 layered double hydroxides: preparation, characterization and application in dyes removal. Mater Today Proc 37:3871–3875. https://doi.org/10.1016/j.matpr.2020.08.460

Fetimi A, Daas A, Benguerba Y, Merouani S, Hamachi M, Kebiche-Senhadji O, Hamdaoui O (2021) Optimization and prediction of safranin-O cationic dye removal from aqueous solution by emulsion liquid membrane (ELM) using artificial neural network-particle swarm optimization (ANN-PSO) hybrid model and response surface methodology (RSM). J Environ Chem Eng 9:105837. https://doi.org/10.1016/j.jece.2021.105837

Friedman J, Hastie T, Tibshirani R (2000) Additive logistic regression: a statistical view of boosting (With discussion and a rejoinder by the authors). Ann Stat 28:337–407. https://doi.org/10.1214/aos/1016218223

Ghaedi M, Ghaedi AM, Hossainpour M, Ansari A, Habibi MH, Asghari AR (2014) Least square-support vector (LS-SVM) method for modeling of methylene blue dye adsorption using copper oxide loaded on activated carbon: kinetic and isotherm study. J Ind Eng Chem 20:1641–1649. https://doi.org/10.1016/j.jiec.2013.08.011

Ghemit R, Boutahala M, Kahoul A (2017) Removal of diclofenac from water with calcined ZnAlFe-CO_3 layered double hydroxides: effect of contact time, concentration, pH and temperature. Desalin Water Treat 83:75–85. https://doi.org/10.5004/dwt.2017.21031

Gijin Kv, Chen YL, Bv O, Gong S, de Wilt HA, Rijnaarts HHM, Langenhoff AAM (2021) Optimizing biological effluent organic matter removal for subsequent micropollutant removal. J Environ Chem Eng 9(5):106247. https://doi.org/10.1016/j.jece.2021.106247

Grover A, Mohiuddin I, Malik AK, Aulakh JS, Vikrant K, Kim K-H, Brown RJC (2022) Magnesium/aluminum layered double hydroxides intercalated with starch for effective adsorptive removal of anionic dyes. J Hazard Mater 424:127454. https://doi.org/10.1016/j.jhazmat.2021.127454

Gul A, Ma'amor A, Khaligh NG, Julkapli NM (2022) Recent advancements in the applications of activated carbon for the heavy metals and dyes removal. Chem Eng Res Des 186:276–299. https://doi.org/10.1016/j.cherd.2022.07.051

Guo Y, Zhu Z, Qiu Y, Zhao J (2012) Adsorption of arsenate on Cu/Mg/Fe/La layered double hydroxide from aqueous solutions. J Hazard Mater 239–240:279–288. https://doi.org/10.1016/j.jhazmat.2012.08.075

Gupta VK, Agarwaal S, Ahmad R, Mirza A, Mittal J (2020) Sequestration of toxic congo red dye from aqueous solution using eco-friendly Guar gum/ activated carbon nanocomposite. Int J Biol Macromol 20:33167–33176. https://doi.org/10.1016/j.ijbiomac.2020.05.025

Han J, Zeng HY, Xu S, Chen CR, Liu XJ (2016) Catalytic properties of CuMgAlO catalyst and degradation mechanism in CWPO of methyl orange. Appl Catal Gen 527:72–80. https://doi.org/10.1016/j.apcata.2016.08.015

Ismail GA, Sakai H (2022) Review on effect of different type of dyes on advanced oxidation processes (AOPs) for textile color removal. Chemosphere 291:132906. https://doi.org/10.1016/j.chemosphere.2021.132906

Jain R, Sharma P, Sikarwar S, Mittal J, Pathak D (2014) Adsorption kinetics and thermodynamics of hazardous dye Tropaeoline 000 unto Aeroxide Alu C (Nano alumina): a non-carbon adsorbent. Desalin Water Treat 52:7776–7783. https://doi.org/10.1080/19443994.2013.837009

Januário EFD, Vidovix TB, NdeCL B, Paixão RM, da Silva LHBR, Homem NC, Bergamasco R, Vieira AMS (2021) Advanced graphene oxide-based membranes as a potential alternative for dyes removal: a review. Sci Total Environ 789:147954. https://doi.org/10.1016/j.scitotenv.2021.147957

Karimifard S, Moghaddam MRA (2018) Application of response surface methodology in physicochemical removal of dyes from

wastewater: a critical review. Sci Total Environ 640–641:772–797. https://doi.org/10.1016/j.scitotenv.2018.05.355

Kazeem TS, Zubair M, Daud M, Al-Harthi MA (2020) Enhanced removal of Eriochrome Black T using graphene/NiMgAl-layered hydroxides: isotherm, kinetic, and thermodynamic studies. Arab J Sci Eng 45:7175–7189. https://doi.org/10.1007/s13369-019-04327-2

Kiwaan HA, Atwee TM, Azab EA, El-Bindary AA (2020) Photocatalytic degradation of organic dyes in the presence of nanostructured titanium dioxide. J Mol Struct 1200:127115. https://doi.org/10.1016/j.molstruc.2019.127115

Kooh MRR, Thotagamuge R, Chau YFC, Mahadi AH, Lim CM (2022) Machine learning approaches to predict adsorption capacity of Azolla pinnata in the removal of methylene blue. J Taiwan Inst Chem Eng 132:104134. https://doi.org/10.1016/j.jtice.2021.11.001

Kumar V, Saharan P, Sharma AK, Umar A, Kaushal I, Mittal A, Al-Hadeethi Y, Rashad B (2020) Silver doped manganese oxide-carbon nanotube nanocomposite for enhanced dye-sequestration: isotherm studies and RSM modelling approach. Ceram Int 46:10309–10319. https://doi.org/10.1016/j.ceramint.2020.01.025

Kumari V, Kumar N, Yadav S, Mittal A, Sharma S (2019) Novel mixed metal oxide ($ZnO.La_2O_3.CeO_2$) synthesized via hydrothermal and solution combustion process – a comparative study and their photocatalytic properties. Mater Today proc 19:650–657. https://doi.org/10.1016/j.matpr.2019.07.748

Lacson CFZ, Lu MC, Huang YH (2022) Calcium-based seeded precipitation for simultaneous removal of fluoride and phosphate: its optimization using BBD-RSM and defluoridation mechanism. J Water Process Eng 47:102658. https://doi.org/10.1016/j.jwpe.2022.102658

Li M, Wu G, Liu Z, Xi X, Xia Y, Ning J, Yang D, Dong A (2020) Uniformly coating ZnAl layered double oxide nanosheets with ultra-thin carbon by ligand and phase transformation for enhanced adsorption of anionic pollutants. J Hazard Mater 397:122766. https://doi.org/10.1016/j.jhazmat.2020.122766

Machrouhi A, Taoufik N, Elhalil A, Tounsadi H, Rais Z, Barka N (2022) Patent Blue V dye adsorption by fresh and calcined Zn/Al LDH: effect of process parameters and experimental design optimization. J Compos Sci 6:115. https://doi.org/10.3390/jcs6040115

Mariyam A, Mittal J, Sakina F, Baker RT, Sharma AK, Mittal A (2021) Efficient batch and Fixed-Bed sequestration of a basic dye using a novel variant of ordered mesoporous carbon as adsorbent. Arabian J Chem 14:103186. https://doi.org/10.1016/j.arabjc.2021.103186

Mazaheri H, Ghaedi M, Ahmadi Azqhandi MH, Asfaram A (2017) Application of machine/statistical learning, artificial intelligence and statistical experimental design for the modeling and optimization of methylene blue and Cd(ii) removal from a binary aqueous solution by natural walnut carbon. Phys Chem Chem Phys 19:11299. https://doi.org/10.1039/C6CP08437K

Meng Y, Luo W, Xia S, Ni Z (2017) Preparation of salen–metal complexes (metal = Co or Ni) intercalated ZnCr-LDHs and their photocatalytic degradation of rhodamine B. Catalysts 7:143. https://doi.org/10.3390/catal7050143

Mittal J (2020) Permissible synthetic food dyes in India. Reson J Sci Educ 25:567–577. https://doi.org/10.1007/s12045-020-0970-6

Mittal J (2021) Recent progress in the synthesis of layered double hydroxides and their application for the adsorptive removal of dyes: a review. J Environ Manage 295:113017. https://doi.org/10.1016/j.jenvman.2021.113017

Mittal A, Mittal J (2015) Hen feather: a remarkable adsorbent for dye removal. Green Chemistry for Dyes Removal from Wastewater. In: Sanjay K. Sharma (ed) Green chemistry for dyes removal from wastewater 409–457. https://doi.org/10.1002/9781118721001.ch11

Mossavi E, Hosseini Sabzevari M, Ghaedi M, Ahmadi Azqhandi MH (2022) Adsorption of the azo dyes from wastewater media by a renewable nanocomposite based on the graphene sheets and hydroxyapatite/ ZnO nanoparticles. J Mol Liq 350:118568. https://doi.org/10.1016/j.molliq.2022.118568

Nada AA, Tantawy HR, Elsayed MA, Bechelany M, Elmowafy ME (2018) Elaboration of nanotitania-magnetic reduced graphene oxide for degradation of tartrazine dye in aqueous solution. Solid State Sci 78:116–125. https://doi.org/10.1016/j.solidstatesciences.2018.02.014

Ouassif H, Moujahid EM, Lahkale R, Sadik R, Bouragba FZ, Sabbar EM, Diouri M (2019) Zinc-aluminum layered double hydroxide: high efficient removal by adsorption of tartrazine dye from aqueous solution. Surf Interfaces 18:100401. https://doi.org/10.1016/j.surfin.2019.100401

Pan X, Zhang M, Liu H, Ouyang S, Ding N, Zhang P (2020) Adsorption behavior and mechanism of Acid Orange 7 and Methylene Blue on self-assembled three dimensional MgAl layered double hydroxide: experimental and DFT investigation. Appl Surf Sci 522:146370. https://doi.org/10.1016/j.apsusc.2020.146370

Parida K, Mohapatra L, Baliarsingh N (2013) Effect of Co^{2+} substitution in the framework of carbonate intercalated Cu/Cr LDH on structural, electronic, optical, and photocatalytic properties. J Phys Chem C 2012 116(42):22417–22424. https://doi.org/10.1021/jp307353f

Pathak N, Ghosh PS, Gupta SK, Kadam RM, Arya A (2016) Defects induced changes in the electronic structures of MgO and their correlation with the optical properties: a special case of electron–hole recombination from the conduction band. RSC Adv 6:96398–96415. https://doi.org/10.1039/C6RA21065A

Quinto ML, Khan S, Picasso G, Sotomayor MDPT (2020) Synthesis, characterization, and evaluation of a selective molecularly imprinted polymer for quantification of the textile dye acid violet 19 in real water samples. J Hazard Mater 384:121374. https://doi.org/10.1016/j.jhazmat.2019.121374

Ramos DKC, Gonzalez MV, Munoz RAE, Cruz JS, De Moure-Flores FJ, Mayén-Hernandez SA (2020) Obtaining and characterization of TiO_2-GO composites for photocatalytic applications. Int J Photoenergy 2020:1–9. https://doi.org/10.1155/2020/3489218

Ratshiedana R, Fakayode OJ, Mishra AK, Kuvarega AT (2021a) Visible-light photocatalytic degradation of tartrazine using hydrothermal synthesized Ag-doped TiO_2 nanoparticles. J Water Process Eng 44:102372. https://doi.org/10.1016/j.jwpe.2021.102372

Ratshiedana R, Fakayode OJ, Mishra AK, Kuvarega AT (2021b) Visible-light photocatalytic degradation of tartrazine using hydrothermal synthesized Ag-doped TiO_2 nanoparticles. J Water Process Eng 44:102372. https://doi.org/10.1016/j.jwpe.2021.102372

Rizi NS, Shahzeydi A, Ghiaci M, Zhang L (2020) Photocatalytic degradation of cationic and anionic organic pollutants in water via Fe-g-C_3N_4/CF as a macroscopic photo-Fenton catalyst under visible light irradiation. J Environ Chem Eng 8:104219. https://doi.org/10.1016/j.jece.2020.104219

Sadiq M, Elhalil A, Abdennouri M, Barka N, Bensitel M, Lamonier C (2021) Effect of aluminium incorporation on physicochemical properties and patent blue V photodegradation of magnesium phosphate materials. Bull Mater Sci 44:1–10. https://doi.org/10.1007/s12034-020-02312-2

Saharan P, Kumar V, Mittal J, Sharma V, Sharma AK (2021) Efficient ultrasonic assisted adsorption of organic pollutants employing bimetallic-carbon nanocomposites. Separation Sci Technol 56:2895–2908. https://doi.org/10.1080/01496395.2020.1866608

Sahnoun S, Boutahala M, Tiar C, Kahoul A (2018) Adsorption of tartrazine from an aqueous solution by octadecyltrimethylammonium bromide-modified bentonite: kinetics and isotherm modeling. C.R. Chim 21:391–398. https://doi.org/10.1016/j.crci.2018.01.008

Shao M, Han J, Wei M, Evans DG, Duan X (2011) The synthesis of hierarchical Zn-Ti layered double hydroxide for efficient visible-light photocatalysis. Chem Eng J 168:519–524. https://doi.org/10.1016/j.cej.2011.01.016

Sharma AK, Sharma Y (2013) p-Toluene sulfonic acid doped polyaniline carbon nanotube composites: synthesis via different routes and modified properties. J Electrochem Sci Eng 3:47–56. https://doi.org/10.5599/jese.2013.0029

Sharma AK, Singh I (2009) A rapid spectrophotometric method for trace determination of zinc. Food Anal Methods 2:311–316. https://doi.org/10.1007/s12161-009-9083-2

Soares APde MR, Carvalho FO, Silva CEF, Gonçalves AHS, Abud AKS (2020) Random Forest as a promising application to predict basic-dye biosorption process using orange waste. J Environ Chem Eng 103952. https://doi.org/10.1016/j.jece.2020.103952

Soufi A, Hajjaoui H, Elmoubarki R, Abdennouri M, Qourzal S, Barka N (2022) Heterogeneous Fenton-like degradation of tartrazine using $CuFe_2O_4$ nanoparticles synthesized by sol-gel combustion. Appl Surf Sci Adv 9:100251. https://doi.org/10.1016/j.apsadv.2022.100251

Souza IPAF, Crespo LHS, Spessato L, Melo SAR, Martins AF, Cazetta AL, Almeida VC (2021) Optimization of thermal conditions of sol-gel method for synthesis of TiO2 using RSM and its influence on photodegradation of tartrazine yellow dye. J Environ Chem Eng 9:104753. https://doi.org/10.1016/j.jece.2020.104753

Srilakshmi C, Thirunavukkarasu T (2019) Enhanced adsorption of Congo red on microwave synthesized layered Zn-Al double hydroxides and its adsorption behaviour using mixture of dyes from aqueous solution. Inorg Chem Commun 100:107–117. https://doi.org/10.1016/j.inoche.2018.12.027

Su M, Xu R, Chen Z, Tang J, Ji C, Yang M, Liu Y, Zhang H, Chen D (2020) Heterostructured $Bi_2O_2CO_3$/rGO/PDA photocatalysts with superior activity for organic pollutant degradation: Structural characterization, reaction mechanism and economic assessment. Ecotoxicol Environ Saf 204:111112. https://doi.org/10.1016/j.ecoenv.2020.111112

Suppaso C, Pongkan N, Intachai S, Ogawa M, Khaorapapong N (2021) Magnetically recoverable β-$Ni(OH)_2$/γ-Fe_2O_3/NiFe-LDH composites; isotherm, thermodynamic and kinetic studies of synthetic dye adsorption and photocatalytic activity. Appl Clay Sci 231:106115. https://doi.org/10.1016/j.clay.2021.106115

Taher T, Putra R, Palapa NR, Lesbani A (2021) Preparation of magnetite-nanoparticle-decorated NiFe layered double hydroxide and its adsorption performance for congo red dye removal. Chem Phys Lett 777:138712. https://doi.org/10.1016/j.cplett.2021.138712

Taoufik N, Sadiq M, Abdennouri M, Qourzal S, Khataee A, Sillanpää M, Barka N (2022) Recent advances in the synthesis and environmental catalytic applications of layered double hydroxides-based materials for degradation of emerging pollutants through advanced oxidation processes. Mater Res Bull 154:111924. https://doi.org/10.1016/j.materresbull.2022.111924

Teotia M, Mittal A, Soni RK (2019) Chapter 3- Light-mediated thermoset polymers. Materials for Biomedical Engineering: Thermoset and Thermoplastic Polymers 57–103. https://doi.org/10.1016/B978-0-12-816874-5.00003-7

Tu VA, Tuan VA (2018) A facile and fast solution chemistry synthesis of porous ZnO nanoparticles for high efficiency photodegradation of tartrazine. Vietnam J Chem 56:214–219. https://doi.org/10.1002/vjch.201800016

Wei L, Yuan Z, Zhong Y, Yang L, Hu X, Zhang Y (2019) An improved gradient boosting regression tree estimation model for soil heavy metal (Arsenic) pollution monitoring using hyperspectral remote sensing. Appl Sci 9:1943. https://doi.org/10.3390/app9091943

Ye Z, Li J, Zhou M, Wang H, Ma Y, Huo P, Yu L, Yan Y (2016) Well-dispersed nebula-like ZnO/CeO_2@HNTs heterostructure for efficient photocatalytic degradation of tetracycline. Chem Eng J 304:917–933. https://doi.org/10.1016/j.cej.2016.07.014

Yuan X, Li W (2017) Graphitic-C_3N_4 modified ZnAl-layered double hydroxides for enhanced photocatalytic removal of organic dye. Appl Clay Sci 138:107–113. https://doi.org/10.1016/j.clay.2017.01.004

Zhang L, Li L, Sun X, Liu P, Yang D, Zhao X (2016) ZnO-layered double Hydroxide@Graphitic carbon nitride composite for consecutive adsorption and photodegradation of dyes under UV and visible lights. Materials 9:1–16. https://doi.org/10.3390/ma9110927

Zhang D, Qian L, Mao B, Huang C, Huang B, Si Y (2018a) A data-driven design for fault detection of wind turbines using random forest and XGboost. IEEE Access 6:21020–21031. https://doi.org/10.1109/ACCESS.2018.2818678

Zhang T, Souza IPAF, Xu J, Almeida VC, Asefa T (2018b) Mesoporous graphitic carbon nitrides decorated with Cu nanoparticles: efficient photocatalysts for degradation of tartrazine yellow dye. Nanomaterials 8:1–14. https://doi.org/10.3390/nano8090636

Zhang Z, Hua Z, Lang J, Song Y, Zhang Q, Han Q, Fan H, Gao M, Li X, Yang J (2019) Eco-friendly nanostructured Zn–Al layered double hydroxide photocatalysts with enhanced. R Soc Chem 21:4607–4619. https://doi.org/10.1039/C9CE00530G

Zhu J, Zhu Z, Zhang H, Lu H, Qiu Y, Zhu L, Küppers S (2016) Enhanced photocatalytic activity of Ce-doped Zn-Al multi-metal oxide composites derived from layered double hydroxide precursors. J Colloid Interface Sci 481:144–157. https://doi.org/10.1016/j.jcis.2016.07.051

Zubair M, Aziz HA, Ihsanullah I, Ahmad MA, Al-Harthi MA (2022) Enhanced removal of Eriochrome Black T from water using biochar/layered double hydroxide/chitosan hybrid composite: performance evaluation and optimization using BBD-RSM approach. Environ Res 209:112861. https://doi.org/10.1016/j.envres.2022.112861

Authors and Affiliations

Nawal Taoufik[1] · Fatima Zahra Janani[1] · Habiba Khiar[1] · Mhamed Sadiq[1] · Mohamed Abdennouri[1] · Mika Sillanpää[2,3,4,5] · Mounia Achak[6,7] · Noureddine Barka[1]

1 Sultan Moulay Slimane University of Beni Mellal, Research Group in Environmental Sciences and Applied Materials (SEMA), FP Khouribga, Morocco

2 Department of Chemical Engineering, School of Mining, Metallurgy and Chemical Engineering, University of Johannesburg, P.O. Box 17011, Doornfontein 2028, South Africa

3 Chemistry Department, College of Science, King Saud University, Riyadh 11451, Saudi Arabia

4 Department of Applied Physics, Faculty of Science and Technology, Universiti Kebangsaan Malaysia, 43600 Bangi, Selangor, Malaysia

5 Department of Biological and Chemical Engineering, Aarhus University, Nørrebrogade 44, 8000 Aarhus C, Denmark

6 Science Engineer Laboratory for Energy, National School of Applied Sciences, Chouaïb Doukkali University, El Jadida, Morocco

7 Chemical & Biochemical Sciences, Green Process Engineering, CBS, Mohammed VI Polytechnic University, Ben Guerir, Morocco